Available online at www.sciencedirect.com
ScienceDirect
Journal of Sound and Vibration 324 (2009) 490–513
JOURNAL OF SOUND AND VIBRATION
www.elsevier.com/locate/jsvi

Flutter suppression of a high aspect-ratio wing with multiple control surfaces

Y.H. Zhao*

Institute of Vibration Engineering Research, Nanjing University of Aeronautics and Astronautics, 210016 Nanjing, People's Republic of China

Received 2 May 2008; received in revised form 7 December 2008; accepted 22 February 2009
Handling Editor: L.G. Tham
Available online 5 April 2009

Abstract

This paper presents a systematic study on active flutter suppression of a high aspect-ratio wing with multiple control surfaces distributed throughout the span. The dynamic characterization of the wing structure is done by the finite element method. Doublet lattice method is used to model unsteady aerodynamic loads acting on the lifting surface with leading-edge and trailing-edge control surfaces. The open-loop aeroelastic equations with input delays are established by the modal transformation of the structural equations and the minimum state approximation of the aerodynamic influence coefficient matrix. To suppress flutter of the time-delayed system, a dynamic controller is synthesized in H_∞ control theory framework. The delay-dependent stability of the closed-loop system is analyzed by tracing the rightmost eigenvalues of the system. Numerical simulations are made to demonstrate the effectiveness of all the above approaches.

1. Introduction

Flutter is a self-excited dynamic instability phenomenon in aeroelasticity. It is caused by the interactions between motions of an aircraft structure and aerodynamic loads. Flutter instability may decrease aircraft performance or even lead to the catastrophic failure of the structure [1]. The traditional passive means of avoiding flutter, such as mass balancing and local stiffening, have continued to the present day. These techniques are usually inefficient (because they add weight to the structure) as well as unsystematic, and they do not always succeed. In order to overcome the inadequacy of passive techniques and to fly at a velocity greater than the flutter velocity, a new technique, called active flutter suppression, was developed in early 1970s. In active flutter suppression, flutter is suppressed through the pitching motions of the control surfaces actuated by an onboard automatic control system.

With the development of control theories, many advanced control strategies, such as optimal control [2], robust control [3] and adaptive control [4], have been applied to the design of the flutter suppression system. However, in most of the previous studies in aeroservoelasticity, time delays in control loops were not considered in the mathematical model of the control system. In fact, some short time delays in control loops

*Tel.: +86 25 84891672; fax: +86 25 84892103.
E-mail address: zyhae@nuaa.edu.cn

0022-460X/$ - see front matter © 2009 Elsevier Ltd. All rights reserved.
doi:10.1016/j.jsv.2009.02.026

Nomenclature

$\bar{a}$	dimensionless distance of the elastic axis from mid-chord, positive aft
$\bar{\mathbf{A}}_{\text{aic}}$	aerodynamic influence coefficient matrix, $\bar{\mathbf{A}}_{\text{aic}} = \bar{\mathbf{D}}_{\text{aic}}^{-1}$
$\mathbf{A}_N$	infinitesimal generator of the solution operator
b_R	reference semi-chord length, $b_R > 0$
$\bar{c}^{\text{LE}}$	dimensionless distance between leading-edge hinge line and mid-chord of the wing, $\bar{c}^{\text{LE}} < 0$
$\bar{c}^{\text{TE}}$	dimensionless distance between trailing-edge hinge line and mid-chord of the wing, $\bar{c}^{\text{TE}} > 0$
$\bar{\mathbf{C}}_{\text{p}}^{\text{cont}}$	pressure coefficients of the aerodynamic boxes on the control surfaces
$\bar{\mathbf{C}}_{\text{p}}^{\text{wing}}$	pressure coefficients of the aerodynamic boxes on the main wing
$\mathbf{D}_{ww}$	modal damping matrix
$\mathbf{D}_{ww}^{a}$	global damping matrix of the wing structure
$\mathbf{D}_{ww}^{s}$	structural damping matrix
$\bar{\mathbf{D}}_{\text{aic}}$	aerodynamic influence coefficient matrix
EI	bending stiffness of the wing
$\mathbf{f}_a$	aerodynamic forces
$\bar{\mathbf{f}}_{\text{f}}^{\text{cont}}$	aerodynamic forces acting on the control surfaces
$\bar{\mathbf{f}}_{\text{f}}^{\text{wing}}$	aerodynamic forces acting on the main wing
f_F	flutter frequency
GJ	torsional stiffness of the wing
$\bar{\mathbf{G}}_{\text{act}}(s)$	transfer function of the actuator system
h	vertical bending deflection of the elastic axis, positive upward
k	reduced frequency
$\mathbf{K}_{ww}$	modal stiffness matrix
$\mathbf{K}_{\text{con}}(s)$	transfer function of the controller
$\bar{\mathbf{K}}_{\text{con}}(s)$	transfer function of the reduced order controller
$\mathbf{K}_{ww}^{a}$	global stiffness matrix of the wing structure
$\mathbf{K}_{ww}^{s}$	structural stiffness matrix
l_n	length of nth finite element
$\mathbf{M}_{ww}$	modal mass matrix
$\mathbf{M}_{wc}$	coupling modal matrix
$\mathbf{M}_{ww}^{a}$	global mass matrix
$\mathbf{M}_{ww}^{s}$	structural mass matrix
$\mathbf{M}_{wc}^{s}$	structural coupling mass matrix
$\bar{\mathbf{P}}_{\text{sys}}(s)$	transfer function of the aeroelastic system
q_d	dynamic pressure
$\mathbf{q}$	modal displacement
$\mathbf{Q}_{wc}(k)$	aerodynamic matrix due to the motions of the control surfaces
$\mathbf{Q}_{ww}(k)$	aerodynamic matrix due to the motion of the main wing
$\mathbf{S}_{acc}$	position matrix reflecting the location of sensors
t	time
$\mathbf{u}_{3/4}^{\text{wing}}$	deflection at the 3/4 chord point of each box on the main wing
$\mathbf{u}_{1/4}^{\text{wing}}$	deflection at the 1/4 chord point of each box on the main wing
$\mathbf{u}_{3/4}^{\text{cont}}$	deflection at the 3/4 chord point of each box on control surfaces
$\mathbf{u}_{1/4}^{\text{cont}}$	deflection at the 1/4 chord point of each box on control surfaces
$\mathbf{U}_{ac}(t)$	actual input signal to the actuators
$U_{\text{step}}(\cdot)$	heavisides step function
V	flow speed
V_F	flutter speed
w	vertical displacement of the wing
$\mathbf{w}$	global vector of nodal displacements
$\mathbf{W}_{\text{act}}$	weighting function to limit the magnitude and frequency content of the actuator inputs
$\mathbf{W}_{\text{noise}}$	weighting function of the noise
$\mathbf{W}_{\text{per}}$	performance weighting function
$\bar{\mathbf{W}}_{3/4}^{\text{wing}}$	dimensionless downwash at the 3/4 chord of the aerodynamic elements on the main wing
$\bar{\mathbf{W}}_{3/4}^{\text{cont}}$	dimensionless downwash at the 3/4 chord of the aerodynamic elements on control surfaces
$\mathbf{X}_a$	aerodynamic states
$\mathbf{Y}_{ae}(t)$	measurement signal
$\mathbf{Y}_{ac}(t)$	output signal of the actuators
$\mathbf{Y}_{\text{per}}(t)$	performance signal
$\mathbf{\Phi}$	modal shape matrix
α	torsional angle of the elastic axis, positive nose-up
α_m	twist angle at the mth node
$\boldsymbol{\beta}$	control surfaces deflection
β^{LEI}	LEI control surface deflection
β^{TEI}	TEI control surface deflection
β^{LEO}	LEO control surface deflection
β^{TEO}	TEO control surface deflection
β_{ac}^{LEI}	commanded signals of the LEI control surface
β_{ac}^{TEI}	commanded signals of the TEI control surface

β_{ac}^{LEO}	commanded signals of the LEO control surface	ω	vibration frequency
		ρ_a	air density
β_{ac}^{TEO}	commanded signals of the TEO control surface	τ, τ_m	time delay

are inevitable because of the dynamics involved in the actuators, sensors, and controllers. The time delays are prevalent when digital controllers, analogue anti-aliasing and reconstruction filters, and hydraulic actuators are used [5]. These time delays become particularly significant when the control effort demands large control forces or high frequencies. It is therefore crucial to understand the effect of time delays on control systems. On the one hand, applications of unsynchronized control forces due to time delay may result in a degradation of the control performance and it may even render the controlled structures to be unstable, but on the other hand, an appropriate time delay may stabilize an unstable system [6].

In the field of aeroservoelasticity, the stability and stabilization of the aeroelastic system with time-delayed feedback control have received much attention in recent years. In Ref. [7], for example, the chaotic motions of a two-dimensional airfoil with cubic pitching stiffness and linear viscous damping were controlled by using the time-delayed feedback in the form of Pyragas. Four control strategies were implemented with plunging displacement, plunging velocity, pitching angle and pitching velocity as the feedback signals. The study showed that the system could be stabilized to a periodic motion if the control was generated by either measuring the plunging displacement, or pitching angle, or pitching velocity. The results demonstrated that the feedback control signal derived from the measurement of the pitching variables is more effective in controlling the chaotic motion of the airfoil. Yuan et al. [8] investigated the effect of the time-delayed feedback control on the flutter instability boundary of a two-dimensional supersonic lifting surface. They demonstrated that the time delay in the nonlinear feedback control could have a profound effect on the stability of the bifurcation motions. For example, it could transform a subcritical Hopf bifurcation to a superciritical one. In Ref. [9] the effects of time delay on the feedback control of two-dimensional lifting surfaces in an incompressible flow-field was investigated. The stability behavior of aeroelastic systems with nonlinear time-delayed feedback was analyzed via Pontryagin's approach in conjunction with Stepan's theorems and the associated aeroelastic Volterra kernels. It was found that, with proper design, the time delay could be a more efficient way to control instability than the conventional control strategies without time delay. In Ref. [10], the flutter instability of actively controlled airfoils involving a time-delayed feedback control was investigated via Stepan's theorems. It was observed that any value of time delay could be detrimental from the point of view of the aeroelastic response, but short time delays might be beneficial from the point of view of flutter instability. In Ref. [11], the center manifold reduction and normal form theory were applied to investigate the stability of an airfoil in the post-flutter flight speed regimes. Numerical simulations were carried out to determine the implications of time delay in the considered controls.

One the other hand, flexible wings for high performance aircraft usually use multiple leading and trailing edge control surfaces to gain multiple benefits [12,13], such as increased control power, reduced aerodynamic drag, reduced aircraft structural weight, and so on. However, the wings of this configuration usually have lower flutter speed due to their flexibility. Hence, flutter suppression of the wings with multiple control surfaces should be studied to increase the flight envelope of the high performance aircraft. However, to the best of our knowledge, the studies that deal with this subject are very limited in the published literature.

In this paper, some theoretical aspects encountered in the design of the active flutter suppression system for a high aspect-ratio wing with multiple control surfaces are studied. We extend the previous studies in the following five aspects: (1) multiple control surfaces configuration is considered in the present study. (2) In Refs. [7,8,10,11], time delay effects on the stability of the controlled aeroelastic system are investigated. However, no control surface and actuator dynamics are considered. As a result, the way by which the control efforts act on the aeroelastic system is not clear. In this paper, time delays in the control loop are introduced into the design procedure of the present flutter suppression system with multiple control surfaces driven by actuators. (3) On the basis of the doublet lattice method (DLM), the unsteady aerodynamic forces model suitable for the multiple control surfaces configuration is also developed. (4) The dynamic control law for the

aeroelastic system with input time delay in control loop is designed by using H_∞ control theory. (5) The delay-dependent stability of the closed-loop system is predicted through the computation of the rightmost eigenvalues of the system.

2. Structural model

As shown in Fig. 1, the wing under analysis is a high aspect-ratio wing. Respectively two inner and outer leading (LEI and LEO) and trailing-edge (TEI and TEO) control surfaces are installed at two different spanwise sections, resulting in four total control surfaces. Each control surface is actuated by a discrete actuator. A finite element representation is used to develop the dynamic structural model of the flexible wing. The flexible wing structure is approximated by a cantilevered beam with a center of mass offset from its neutral axis. Along with Euler–Bernoulli bending, the flexible model also incorporates torsion. Therefore, a beam-rod finite element model of the structure is developed which acts like a beam in bending and a rod in torsion. The elastic axis is chosen to be the neutral axis of the beam so that the bending and torsion of the straight wing structure are structurally uncoupled statically. Fig. 1 shows a finite element mesh for the wing model consisting of n_e elements. Each beam-rod element has six degrees-of-freedom, three degrees-of-freedom at each node. These include one translational degree degrees-of-freedom, bending displacement, and two rotational degrees of freedom which describe the bending slope and the torsional motion about the elastic axis, respectively.

As shown in Fig. 2, the displacement of the lifting surface can be represented by a vertical bending deflection $h(y, t)$ (positive, upward) along the elastic axis and a twist angle $\alpha(y, t)$ (positive, nose-up) about that axis, given by

$$w(x, y, t) = h(y, t) - (x - \bar{a} \cdot b)\alpha(y, t) - \mathbf{U}_{\text{cont}}^{\text{T}}(x, y)(\boldsymbol{\beta}(t) + \boldsymbol{\alpha}_{\text{cont}}(y, t)), \tag{1}$$

where $\mathbf{U}_{\text{cont}}$, $\boldsymbol{\beta}(t)$ and $\boldsymbol{\alpha}_{\text{cont}}(y, t)$ are given in Appendix A.

For convenience, we introduce two finite element sets denoted by SETO and SETI, respectively. SETOconsists of the elements located in the span of LEO (or TEO) control surface. SETI consists of the elements located in the span of LEI (or TEI) control surface. The relative deflections of control surfaces can be written as

$$\begin{cases} \beta_{\text{span}}^{\text{LEI}}(y, t) = \beta^{\text{LEI}}(t) + f(y, t), \\ \beta_{\text{span}}^{\text{TEI}}(y, t) = \beta^{\text{TEI}}(t) + f(y, t), \\ \beta_{\text{span}}^{\text{LEO}}(y, t) = \beta^{\text{LEO}}(t) + g(y, t), \\ \beta_{\text{span}}^{\text{TEO}}(y, t) = \beta^{\text{TEO}}(t) + g(y, t), \end{cases} \tag{2}$$

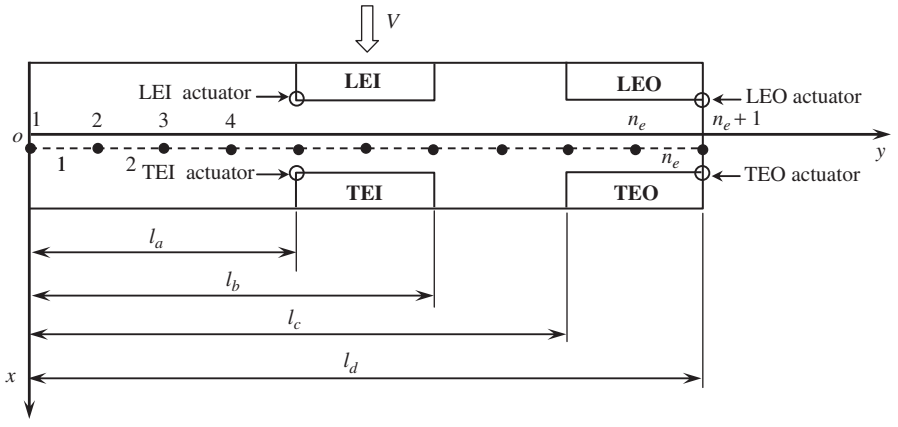

Fig. 1. Structural model of the high aspect-ratio wing.

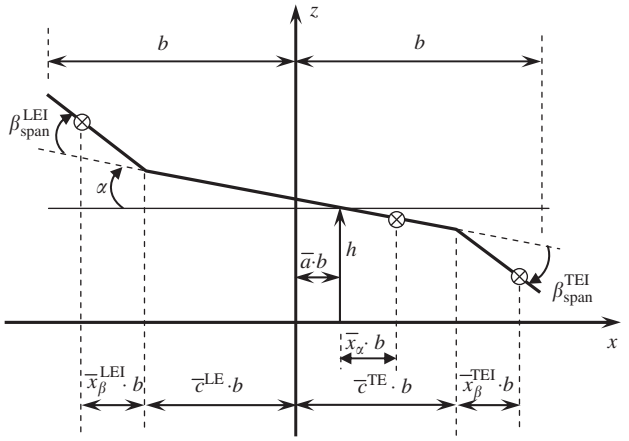

Fig. 2. Cross-section of the wing.

where $f(y, t)$ and $g(y, t)$ are defined as follows:

When $l_a \leqslant y < l_a + l_{[\mathrm{SETI}(1)]}$

$$f(y,t) = \frac{l_a - y}{l_{[\mathrm{SETI}(1)]}}(\alpha_{\mathrm{SETI}(1)+1}(t) - \alpha_{\mathrm{SETI}(1)}(t)), \tag{3}$$

When

$$l_a + \sum_{j=1}^{i-1} l_{[\mathrm{SETI}(j)]} \leqslant y < l_a + \sum_{j=1}^{i} l_{[\mathrm{SETI}(j)]}, \quad i = 2, 3, \ldots, n_I$$

$$f(y,t) = \frac{(l_a + \sum_{j=1}^{i-1} l_{[\mathrm{SETI}(j)]}) - y}{l_{[\mathrm{SETI}(i)]}}(\alpha_{\mathrm{SETI}(i+)1}(t) - \alpha_{\mathrm{SETI}(i)}(t)) + \alpha_{\mathrm{SETI}(i)}(t) - \alpha_{\mathrm{SETI}(1)}(t), \tag{4}$$

When $l_b \leqslant y < l_b + l_{[\mathrm{SETO}(1)]}$

$$g(y,t) = \frac{l_b + l_{[\mathrm{SETO}(1)]} - y}{l_{[\mathrm{SETO}(1)]}}(\alpha_{\mathrm{SETO}(1)+1}(t) - \alpha_{\mathrm{SETO}(1)}(t)) + \alpha_{\mathrm{SETO}(n_o)+1}(t) - \alpha_{\mathrm{SETO}(1)+1}(t), \tag{5}$$

When

$$l_b + \sum_{j=1}^{i-1} l_{[\mathrm{SETO}(j)]} \leqslant y < l_b + \sum_{j=1}^{i} l_{[\mathrm{SETO}(j)]}, \quad i = 2, 3, \ldots, n_o$$

$$g(y,t) = \frac{(l_b + \sum_{j=1}^{i} l_{[\mathrm{SETO}(j)]}) - y}{l_{[\mathrm{SETO}(i)]}}(\alpha_{\mathrm{SETO}(i)+1}(t) - \alpha_{\mathrm{SETO}(i)}(t)) + \alpha_{\mathrm{SETO}(n_o)+1}(t) - \alpha_{\mathrm{SETO}(i)+1}(t), \tag{6}$$

In Eqs. (3), (4), (5) and (6), l_n denotes the length of the nth element, $\alpha_m(t)$ is the twist angle at the mth node. SETI(j) and SETO(j) denote the jth element in the sets of SETI and SETO, respectively. n_o is the number of elements located in the span of LEO (or TEO) control surface, n_I is the number of elements located in the span of LEI (or TEI) control surface.

Upon assembly of the element mass, damping and stiffness matrices, the equations of motion of the wing can be written as

$$\mathbf{M}_{ww}^{s}\ddot{\mathbf{w}} + \mathbf{D}_{ww}^{s}\dot{\mathbf{w}} + \mathbf{K}_{ww}^{s}\mathbf{w} = -\mathbf{M}_{wc}^{s}\ddot{\boldsymbol{\beta}} + \mathbf{f}_a, \tag{7}$$

where $\mathbf{M}_{ww}^{s}$, $\mathbf{D}_{ww}^{s}$, $\mathbf{K}_{ww}^{s}$ and $\mathbf{M}_{wc}^{s}$ are the mass, damping, stiffness and coupling mass matrices, respectively. $\mathbf{W}$ is the global vector of nodal displacements. $\mathbf{f}_a$ is the aerodynamic forces given in the next section.

3. Unsteady aerodynamic model

For calculation of subsonic, compressible unsteady aerodynamic forces on harmonically oscillating lifting surfaces, the most generally used scheme is the DLM [14]. In DLM, the lifting surface is represented by a grid of boxes of trapezoidal shape, as shown in Fig. 3. The DLM determines the pressure in each box as a function of the downwash velocities at the $\frac{3}{4}$-chord locations of the different boxes, where

$$\begin{Bmatrix} \bar{\mathbf{W}}_{3/4}^{\text{wing}} \\ \bar{\mathbf{W}}_{3/4}^{\text{cont}} \end{Bmatrix} = \bar{\mathbf{D}}_{\text{aic}} \begin{Bmatrix} \bar{\mathbf{C}}_{\text{p}}^{\text{wing}} \\ \bar{\mathbf{C}}_{\text{p}}^{\text{cont}} \end{Bmatrix}, \tag{8}$$

where $\bar{\mathbf{D}}_{\text{aic}}$ is the aerodynamic influence coefficient matrix, $\bar{\mathbf{W}}_{3/4}^{\text{wing}}$ is the dimensionless downwash velocities at the $\frac{3}{4}$ chord of aerodynamic boxes on the main wing, $\bar{\mathbf{C}}_{\text{p}}^{\text{wing}}$ is pressure coefficients of the boxes on the main wing.

Downwash velocities $\bar{\mathbf{W}}_{3/4}^{\text{cont}}$ and pressure coefficients $\bar{\mathbf{C}}_{\text{p}}^{\text{cont}}$ for the aerodynamic boxes on control surfaces can be expressed as

$$\bar{\mathbf{W}}_{3/4}^{\text{cont}} = \begin{Bmatrix} \bar{\mathbf{W}}_{3/4}^{\text{LEI}} \\ \bar{\mathbf{W}}_{3/4}^{\text{TEI}} \\ \bar{\mathbf{W}}_{3/4}^{\text{LEO}} \\ \bar{\mathbf{W}}_{3/4}^{\text{TEO}} \end{Bmatrix}, \quad \bar{\mathbf{C}}_{\text{p}}^{\text{cont}} = \begin{Bmatrix} \bar{\mathbf{C}}_{\text{p}}^{\text{LEI}} \\ \bar{\mathbf{C}}_{\text{p}}^{\text{TEI}} \\ \bar{\mathbf{C}}_{\text{p}}^{\text{LEO}} \\ \bar{\mathbf{C}}_{\text{p}}^{\text{TEO}} \end{Bmatrix}. \tag{9}$$

The DLM yields the pressures in each of the boxes in the form:

$$\begin{Bmatrix} \bar{\mathbf{C}}_{\text{p}}^{\text{wing}} \\ \bar{\mathbf{C}}_{\text{p}}^{\text{cont}} \end{Bmatrix} = \bar{\mathbf{A}}_{\text{aic}} \begin{Bmatrix} \bar{\mathbf{W}}_{3/4}^{\text{wing}} \\ \bar{\mathbf{W}}_{3/4}^{\text{cont}} \end{Bmatrix} = \begin{bmatrix} \bar{\mathbf{A}}_{ss} & \bar{\mathbf{A}}_{sc} \\ \bar{\mathbf{A}}_{cs} & \bar{\mathbf{A}}_{cc} \end{bmatrix} \begin{Bmatrix} \bar{\mathbf{W}}_{3/4}^{\text{wing}} \\ \bar{\mathbf{W}}_{3/4}^{\text{cont}} \end{Bmatrix}, \tag{10}$$

where $\bar{\mathbf{A}}_{\text{aic}} = \bar{\mathbf{D}}_{\text{aic}}^{-1}$.

With harmonic motion assumption, the dimensionless downwash velocities $\bar{\mathbf{W}}_{3/4}^{\text{wing}}$ can be written as

$$\bar{\mathbf{W}}_{3/4}^{\text{wing}} = \frac{\partial}{\partial x}\mathbf{u}_{3/4}^{\text{wing}} + \frac{\mathrm{i}k}{b_R}\mathbf{u}_{3/4}^{\text{wing}}, \tag{11}$$

where $k = \omega b_R/V$ is the reduced frequency, b_R is the reference semi-chord length, ω is the vibration frequency, $\mathbf{u}_{3/4}^{\text{wing}}$ is the deflection at the $\frac{3}{4}$ chord point of each box on the main wing. Note that the terms in the right hand side of Eq. (11) are related to structural displacement $\mathbf{w}$ as follows:

$$\frac{\partial}{\partial x}\mathbf{u}_{3/4}^{\text{wing}} = \mathbf{D}_{3/4}^{aw}\mathbf{w}, \quad \mathbf{u}_{3/4}^{\text{wing}} = \mathbf{T}_{3/4}^{aw}\mathbf{w}. \tag{12}$$

Substituting Eq. (12) into Eq. (11), one obtains:

$$\bar{\mathbf{W}}_{3/4}^{\text{wing}} = \left(\mathbf{D}_{3/4}^{aw} + \frac{\mathrm{i}k}{b_R}\mathbf{T}_{3/4}^{aw}\right)\mathbf{w} = \mathbf{E}_{3/4}^{aw}(k)\mathbf{w}. \tag{13}$$

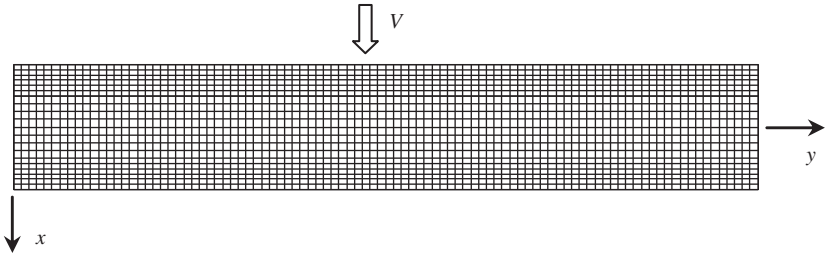

Fig. 3. Aerodynamic boxes on the lifting surface.

The dimensionless downwash velocities $\bar{\mathbf{W}}_{3/4}^{\text{cont}}$ can be written as

$$\bar{\mathbf{W}}_{3/4}^{\text{cont}} = \begin{Bmatrix} \bar{\mathbf{W}}_{3/4}^{\text{LEI}} \\ \bar{\mathbf{W}}_{3/4}^{\text{TEI}} \\ \bar{\mathbf{W}}_{3/4}^{\text{LEO}} \\ \bar{\mathbf{W}}_{3/4}^{\text{TEO}} \end{Bmatrix} = \frac{\partial}{\partial x}\mathbf{u}_{3/4}^{\text{cont}} + \frac{ik}{b_R}\mathbf{u}_{3/4}^{\text{cont}} = \frac{\partial}{\partial x}\begin{Bmatrix} \mathbf{u}_{3/4}^{\text{LEI}} \\ \mathbf{u}_{3/4}^{\text{TEI}} \\ \mathbf{u}_{3/4}^{\text{LEO}} \\ \mathbf{u}_{3/4}^{\text{TEO}} \end{Bmatrix} + \frac{ik}{b_R}\begin{Bmatrix} \mathbf{u}_{3/4}^{\text{LEI}} \\ \mathbf{u}_{3/4}^{\text{TEI}} \\ \mathbf{u}_{3/4}^{\text{LEO}} \\ \mathbf{u}_{3/4}^{\text{TEO}} \end{Bmatrix}, \tag{14}$$

where $\mathbf{u}_{3/4}^{\text{cont}}$ is the deflection at the $\frac{3}{4}$ chord point of each box on control surfaces.

From Eq. (1), we have the following expressions:

$$\begin{cases} \mathbf{u}_{3/4}^{\text{LEI}} = \mathbf{h}_{3/4}^{\text{LEI}} - \mathbf{D}_{3/4\alpha}^{\text{LEI}}\boldsymbol{\alpha}_{3/4}^{\text{LEI}} - \mathbf{D}_{3/4\beta}^{\text{LEI}}\beta^{\text{LEI}} - \bar{\mathbf{D}}_{3/4\beta}^{\text{LEI}}\mathbf{f}_{3/4}^{\text{LEI}}, \\ \mathbf{u}_{3/4}^{\text{TEI}} = \mathbf{h}_{3/4}^{\text{TEI}} - \mathbf{D}_{3/4\alpha}^{\text{TEI}}\boldsymbol{\alpha}_{3/4}^{\text{TEI}} - \mathbf{D}_{3/4\beta}^{\text{TEI}}\beta^{\text{TEI}} - \bar{\mathbf{D}}_{3/4\beta}^{\text{TEI}}\mathbf{f}_{3/4}^{\text{TEI}}, \\ \mathbf{u}_{3/4}^{\text{LEO}} = \mathbf{h}_{3/4}^{\text{LEO}} - \mathbf{D}_{3/4\alpha}^{\text{LEO}}\boldsymbol{\alpha}_{3/4}^{\text{LEO}} - \mathbf{D}_{3/4\beta}^{\text{LEO}}\beta^{\text{LEO}} - \bar{\mathbf{D}}_{3/4\beta}^{\text{LEO}}\mathbf{g}_{3/4}^{\text{LEO}}, \\ \mathbf{u}_{3/4}^{\text{TEO}} = \mathbf{h}_{3/4}^{\text{TEO}} - \mathbf{D}_{3/4\alpha}^{\text{TEO}}\boldsymbol{\alpha}_{3/4}^{\text{TEO}} - \mathbf{D}_{3/4\beta}^{\text{TEO}}\beta^{\text{TEO}} - \bar{\mathbf{D}}_{3/4\beta}^{\text{TEO}}\mathbf{g}_{3/4}^{\text{TEO}}. \end{cases} \tag{15}$$

herein the matrices in Eq. (15) are given in Appendix B. Note that the following expressions hold true:

$$\begin{cases} \dfrac{\partial}{\partial x}\mathbf{u}_{3/4}^{\text{LEI}} = -\boldsymbol{\alpha}_{3/4}^{\text{LEI}} - \mathbf{I}_{\beta}^{\text{LEI}}\beta^{\text{LEI}} - \mathbf{f}_{3/4}^{\text{LEI}}, \\ \dfrac{\partial}{\partial x}\mathbf{u}_{3/4}^{\text{TEI}} = -\boldsymbol{\alpha}_{3/4}^{\text{TEI}} - \mathbf{I}_{\beta}^{\text{TEI}}\beta^{\text{TEI}} - \mathbf{f}_{3/4}^{\text{TEI}}, \\ \dfrac{\partial}{\partial x}\mathbf{u}_{3/4}^{\text{LEO}} = -\boldsymbol{\alpha}_{3/4}^{\text{LEO}} - \mathbf{I}_{\beta}^{\text{LEO}}\beta^{\text{LEO}} - \mathbf{g}_{3/4}^{\text{LEO}}, \\ \dfrac{\partial}{\partial x}\mathbf{u}_{3/4}^{\text{TEO}} = -\boldsymbol{\alpha}_{3/4}^{\text{TEO}} - \mathbf{I}_{\beta}^{\text{TEO}}\beta^{\text{TEO}} - \mathbf{g}_{3/4}^{\text{TEO}}, \end{cases} \tag{16}$$

where

$$\mathbf{I}_{\beta}^{\text{LEI}} = \begin{bmatrix} 1 \\ 1 \\ \vdots \\ 1 \end{bmatrix}_{n^{\text{LEI}}\times 1}, \quad \mathbf{I}_{\beta}^{\text{TEI}} = \begin{bmatrix} 1 \\ 1 \\ \vdots \\ 1 \end{bmatrix}_{n^{\text{TEI}}\times 1}, \quad \mathbf{I}_{\beta}^{\text{LEO}} = \begin{bmatrix} 1 \\ 1 \\ \vdots \\ 1 \end{bmatrix}_{n^{\text{LEO}}\times 1}, \quad \mathbf{I}_{\beta}^{\text{TEO}} = \begin{bmatrix} 1 \\ 1 \\ \vdots \\ 1 \end{bmatrix}_{n^{\text{TEO}}\times 1}.$$

From Eqs. (14), (15) and (16), the downwash velocities of control surfaces can be expressed as

$$\begin{cases} \bar{\mathbf{W}}_{3/4}^{\text{LEI}} = -\boldsymbol{\alpha}_{3/4}^{\text{LEI}} - \mathbf{f}_{3/4}^{\text{LEI}} + \dfrac{ik}{b_R}(\mathbf{h}_{3/4}^{\text{LEI}} - \mathbf{D}_{3/4\alpha}^{\text{LEI}}\boldsymbol{\alpha}_{3/4}^{\text{LEI}} - \bar{\mathbf{D}}_{3/4\beta}^{\text{LEI}}\mathbf{f}_{3/4}^{\text{LEI}}) - \left(\mathbf{I}_{\beta}^{\text{LEI}} + \dfrac{ik}{b_R}\mathbf{D}_{3/4\beta}^{\text{LEI}}\right)\beta^{\text{LEI}}, \\ \bar{\mathbf{W}}_{3/4}^{\text{TEI}} = -\boldsymbol{\alpha}_{3/4}^{\text{TEI}} - \mathbf{f}_{3/4}^{\text{TEI}} + \dfrac{ik}{b_R}(\mathbf{h}_{3/4}^{\text{TEI}} - \mathbf{D}_{3/4\alpha}^{\text{TEI}}\boldsymbol{\alpha}_{3/4}^{\text{TEI}} - \bar{\mathbf{D}}_{3/4\beta}^{\text{TEI}}\mathbf{f}_{3/4}^{\text{TEI}}) - \left(\mathbf{I}_{\beta}^{\text{TEI}} + \dfrac{ik}{b_R}\mathbf{D}_{3/4\beta}^{\text{TEI}}\right)\beta^{\text{TEI}}, \\ \bar{\mathbf{W}}_{3/4}^{\text{LEO}} = -\boldsymbol{\alpha}_{3/4}^{\text{LEO}} - \mathbf{g}_{3/4}^{\text{LEO}} + \dfrac{ik}{b_R}(\mathbf{h}_{3/4}^{\text{LEO}} - \mathbf{D}_{3/4\alpha}^{\text{LEO}}\boldsymbol{\alpha}_{3/4}^{\text{LEO}} - \bar{\mathbf{D}}_{3/4\beta}^{\text{LEO}}\mathbf{g}_{3/4}^{\text{LEO}}) - \left(\mathbf{I}_{\beta}^{\text{LEO}} + \dfrac{ik}{b_R}\mathbf{D}_{3/4\beta}^{\text{LEO}}\right)\beta^{\text{LEO}}, \\ \bar{\mathbf{W}}_{3/4}^{\text{TEO}} = -\boldsymbol{\alpha}_{3/4}^{\text{TEO}} - \mathbf{g}_{3/4}^{\text{TEO}} + \dfrac{ik}{b_R}(\mathbf{h}_{3/4}^{\text{TEO}} - \mathbf{D}_{3/4\alpha}^{\text{TEO}}\boldsymbol{\alpha}_{3/4}^{\text{TEO}} - \bar{\mathbf{D}}_{3/4\beta}^{\text{TEO}}\mathbf{g}_{3/4}^{\text{TEO}}) - \left(\mathbf{I}_{\beta}^{\text{TEO}} + \dfrac{ik}{b_R}\mathbf{D}_{3/4\beta}^{\text{TEO}}\right)\beta^{\text{TEO}}. \end{cases} \tag{17}$$

Displacement of each box on control surfaces can be expressed by structural displacement $\mathbf{w}$, given by

$$\begin{cases} \boldsymbol{\alpha}_{3/4}^{\mathrm{LEI}} = \mathbf{A}_{3/4\alpha}^{\mathrm{LEI}}\mathbf{w}, & \mathbf{h}_{3/4}^{\mathrm{LEI}} = \mathbf{A}_{3/4h}^{\mathrm{LEI}}\mathbf{w}, & \mathbf{f}_{3/4}^{\mathrm{LEI}} = \mathbf{A}_{3/4f}^{\mathrm{LEI}}\mathbf{w}, \\ \boldsymbol{\alpha}_{3/4}^{\mathrm{TEI}} = \mathbf{A}_{3/4\alpha}^{\mathrm{TEI}}\mathbf{w}, & \mathbf{h}_{3/4}^{\mathrm{TEI}} = \mathbf{A}_{3/4h}^{\mathrm{TEI}}\mathbf{w}, & \mathbf{f}_{3/4}^{\mathrm{TEI}} = \mathbf{A}_{3/4f}^{\mathrm{TEI}}\mathbf{w}, \\ \boldsymbol{\alpha}_{3/4}^{\mathrm{LEO}} = \mathbf{A}_{3/4\alpha}^{\mathrm{LEO}}\mathbf{w}, & \mathbf{h}_{3/4}^{\mathrm{LEO}} = \mathbf{A}_{3/4h}^{\mathrm{LEO}}\mathbf{w}, & \mathbf{g}_{3/4}^{\mathrm{LEO}} = \mathbf{A}_{3/4g}^{\mathrm{LEO}}\mathbf{w}, \\ \boldsymbol{\alpha}_{3/4}^{\mathrm{TEO}} = \mathbf{A}_{3/4\alpha}^{\mathrm{TEO}}\mathbf{w}, & \mathbf{h}_{3/4}^{\mathrm{TEO}} = \mathbf{A}_{3/4h}^{\mathrm{TEO}}\mathbf{w}, & \mathbf{g}_{3/4}^{\mathrm{TEO}} = \mathbf{A}_{3/4g}^{\mathrm{TEO}}\mathbf{w}. \end{cases} \tag{18}$$

Substituting Eq. (18) into Eq. (17), one obtains:

$$\bar{\mathbf{W}}_{3/4}^{\mathrm{cont}} = \mathbf{D}_{3/4}^{h\alpha}(k)\mathbf{w} - \mathbf{D}_{3/4}^{\beta}(k)\boldsymbol{\beta}, \tag{19}$$

where the matrices $\mathbf{D}_{3/4}^{h\alpha}(k)$ and $\mathbf{D}_{3/4}^{\beta}(k)$ are given in Appendix C.

Based on Eqs. (10), (13) and (19), the aerodynamic forces acting on the main wing and the control surfaces can be written as

$$\begin{cases} \bar{\mathbf{f}}_{\mathrm{f}}^{\mathrm{wing}} = q_d\mathbf{S}^{\mathrm{wing}}[(\bar{\mathbf{A}}_{ss}\mathbf{E}_{3/4}^{aw}(k) + \bar{\mathbf{A}}_{sc}\mathbf{D}_{3/4}^{h\alpha}(k))\mathbf{w} - \bar{\mathbf{A}}_{sc}\mathbf{D}_{3/4}^{\beta}(k)\boldsymbol{\beta}], \\ \bar{\mathbf{f}}_{\mathrm{f}}^{\mathrm{cont}} = q_d\mathbf{S}^{\mathrm{cont}}[(\bar{\mathbf{A}}_{cs}\mathbf{E}_{3/4}^{aw}(k) + \bar{\mathbf{A}}_{cc}\mathbf{D}_{3/4}^{h\alpha}(k))\mathbf{w} - \bar{\mathbf{A}}_{cc}\mathbf{D}_{3/4}^{\beta}(k)\boldsymbol{\beta}]. \end{cases} \tag{20}$$

where diagonal matrices $\mathbf{S}^{\mathrm{wing}}$ and $\mathbf{S}^{\mathrm{cont}}$ denote the area of aerodynamic boxes on the main wing and control surfaces, respectively. $q_d = 0.5\rho_a V^2$ is dynamic pressure, ρ_a is air density. So the virtual work done by aerodynamic forces can be written as

$$\delta W_a = \delta(\mathbf{u}_{1/4}^{\mathrm{wing}})^{\mathrm{T}}\bar{\mathbf{f}}_{\mathrm{f}}^{\mathrm{wing}} + \delta(\mathbf{u}_{1/4}^{\mathrm{cont}})^{\mathrm{T}}\bar{\mathbf{f}}_{\mathrm{f}}^{\mathrm{cont}}, \tag{21}$$

where $\mathbf{u}_{1/4}^{\mathrm{wing}}$ and $\mathbf{u}_{1/4}^{\mathrm{cont}}$ are deflections at the $\frac{1}{4}$ chord point of the aerodynamic boxes on the main wing and control surfaces, respectively.

Note that the deflections $\mathbf{u}_{1/4}^{\mathrm{wing}}$ and $\mathbf{u}_{1/4}^{\mathrm{cont}}$ are related to the structural displacements $\mathbf{w}$ and the relative deflections of control surfaces $\boldsymbol{\beta}$, given by

$$\mathbf{u}_{1/4}^{\mathrm{wing}} = \mathbf{T}_{1/4}^{aw}\mathbf{w}, \quad \mathbf{u}_{1/4}^{\mathrm{cont}} = \mathbf{D}_{1/4}^{h\alpha}\mathbf{w} - \mathbf{D}_{1/4}^{\beta}\boldsymbol{\beta}, \tag{22}$$

where

$$\mathbf{D}_{1/4}^{h\alpha} = \begin{bmatrix} \mathbf{A}_{1/4h}^{\mathrm{LEI}} - \mathbf{D}_{1/4\alpha}^{\mathrm{LEI}}\mathbf{A}_{1/4\alpha}^{\mathrm{LEI}} - \bar{\mathbf{D}}_{1/4\beta}^{\mathrm{LEI}}\mathbf{A}_{1/4f}^{\mathrm{LEI}} \\ \mathbf{A}_{1/4h}^{\mathrm{TEI}} - \mathbf{D}_{1/4\alpha}^{\mathrm{TEI}}\mathbf{A}_{1/4\alpha}^{\mathrm{TEI}} - \bar{\mathbf{D}}_{1/4\beta}^{\mathrm{TEI}}\mathbf{A}_{1/4f}^{\mathrm{TEI}} \\ \mathbf{A}_{1/4h}^{\mathrm{LEO}} - \mathbf{D}_{1/4\alpha}^{\mathrm{LEO}}\mathbf{A}_{1/4\alpha}^{\mathrm{LEO}} - \bar{\mathbf{D}}_{1/4\beta}^{\mathrm{LEO}}\mathbf{A}_{1/4g}^{\mathrm{LEO}} \\ \mathbf{A}_{1/4h}^{\mathrm{TEO}} - \mathbf{D}_{1/4\alpha}^{\mathrm{TEO}}\mathbf{A}_{1/4\alpha}^{\mathrm{TEO}} - \bar{\mathbf{D}}_{1/4\beta}^{\mathrm{TEO}}\mathbf{A}_{1/4g}^{\mathrm{TEO}} \end{bmatrix}, \quad \mathbf{D}_{1/4}^{\beta} = \begin{bmatrix} \mathbf{D}_{1/4\beta}^{\mathrm{LEI}} & \mathbf{0} & \mathbf{0} & \mathbf{0} \\ \mathbf{0} & \mathbf{D}_{1/4\beta}^{\mathrm{TEI}} & \mathbf{0} & \mathbf{0} \\ \mathbf{0} & \mathbf{0} & \mathbf{D}_{1/4\beta}^{\mathrm{LEO}} & \mathbf{0} \\ 0 & \mathbf{0} & \mathbf{0} & \mathbf{D}_{1/4\beta}^{\mathrm{TEO}} \end{bmatrix}.$$

Substituting Eq. (20) and (22) into Eq. (21), we have:

$$\delta W_a = \delta\mathbf{w}^{\mathrm{T}}\mathbf{f}_a, \tag{23}$$

where

$$\mathbf{f}_a = q_d\mathbf{Q}_{ww}^{s}(k)\mathbf{w} + q_d\mathbf{Q}_{wc}^{s}(k)\boldsymbol{\beta}, \tag{24}$$

$$\mathbf{Q}_{ww}^{s}(k) = (\mathbf{T}_{1/4}^{aw})^{\mathrm{T}}\mathbf{S}^{\mathrm{wing}}(\bar{\mathbf{A}}_{ss}\mathbf{E}_{3/4}^{aw}(k) + \bar{\mathbf{A}}_{sc}\mathbf{D}_{3/4}^{h\alpha}(k)) + (\mathbf{D}_{1/4}^{h\alpha})^{\mathrm{T}}\mathbf{S}^{\mathrm{cont}}(\bar{\mathbf{A}}_{cs}\mathbf{E}_{3/4}^{aw}(k) + \bar{\mathbf{A}}_{cc}\mathbf{D}_{3/4}^{h\alpha}(k)), \tag{25}$$

$$\mathbf{Q}_{wc}^{s}(k) = -(\mathbf{T}_{1/4}^{aw})^{\mathrm{T}}\mathbf{S}^{\mathrm{wing}}\bar{\mathbf{A}}_{sc}\mathbf{D}_{3/4}^{\beta}(k) - (\mathbf{D}_{1/4}^{h\alpha})^{\mathrm{T}}\mathbf{S}^{\mathrm{cont}}\bar{\mathbf{A}}_{cc}\mathbf{D}_{3/4}^{\beta}(k). \tag{26}$$

It can be seen from Eq. (24) that the total aerodynamic forces acting on the wing include two parts. The first part is the aerodynamic force induced by structural displacements and the second part represents the aerodynamic force due to the deflections of control surfaces.

Substituting Eq. (24) into Eq. (7), one obtains:

$$\mathbf{M}^s_{ww}\ddot{\mathbf{w}} + \mathbf{D}^s_{ww}\dot{\mathbf{w}} + \mathbf{K}^s_{ww}\mathbf{w} = -\mathbf{M}^s_{wc}\ddot{\boldsymbol{\beta}} + q_d\mathbf{Q}^s_{ww}(k)\mathbf{w} + q_d\mathbf{Q}^s_{wc}(k)\boldsymbol{\beta}. \tag{27}$$

After taking the boundary conditions of the wing into consideration, we obtain the equations of motion for the wing in physical space:

$$\mathbf{M}^a_{ww}\ddot{\mathbf{w}}^a + \mathbf{D}^a_{ww}\dot{\mathbf{w}}^a + \mathbf{K}^a_{ww}\mathbf{w}^a = -\mathbf{M}^a_{wc}\ddot{\boldsymbol{\beta}} + q_d\mathbf{Q}^a_{ww}(k)\mathbf{w}^a + q_d\mathbf{Q}^a_{wc}(k)\boldsymbol{\beta}. \tag{28}$$

4. Open-loop aeroelastic equations in the time domain

Introducing modal transformation $\mathbf{w}^a = \boldsymbol{\Phi}\mathbf{q}$, where $\boldsymbol{\Phi}$ is modal shape matrix, $\mathbf{q}$ is modal displacement, then Eq. (28) can be written as

$$\mathbf{M}_{ww}\ddot{\mathbf{q}} + \mathbf{D}_{ww}\dot{\mathbf{q}} + \mathbf{K}_{ww}\mathbf{q} = -\mathbf{M}_{wc}\ddot{\boldsymbol{\beta}} + q_d\mathbf{Q}_{ww}(k)\mathbf{q} + q_d\mathbf{Q}_{wc}(k)\boldsymbol{\beta}, \tag{29}$$

where

$$\mathbf{M}_{ww} = \boldsymbol{\Phi}^{\mathrm{T}}\mathbf{M}^a_{ww}\boldsymbol{\Phi}, \quad \mathbf{D}_{ww} = \boldsymbol{\Phi}^{\mathrm{T}}\mathbf{D}^a_{ww}\boldsymbol{\Phi}, \quad \mathbf{K}_{ww} = \boldsymbol{\Phi}^{\mathrm{T}}\mathbf{K}^a_{ww}\boldsymbol{\Phi}, \quad \mathbf{M}_{wc} = \boldsymbol{\Phi}^{\mathrm{T}}\mathbf{M}^a_{wc},$$

$$\mathbf{Q}_{ww}(k) = \boldsymbol{\Phi}^{\mathrm{T}}\mathbf{Q}^a_{ww}(k)\boldsymbol{\Phi}, \quad \mathbf{Q}_{wc}(k) = \boldsymbol{\Phi}^{\mathrm{T}}\mathbf{Q}^a_{wc}(k).$$

For the design of the flutter suppression system, it is necessary to transform the equations of motion into the state-space form. Here, the minimum state method is used for the rational function approximation. It is known that in minimum state method, the increase in the size of the augmented aerodynamic states is much smaller than any other methods. For this purpose, we write Eq. (29) into the following form:

$$[\mathbf{M}_{ww}s^2 + \mathbf{D}_{ww}s + \mathbf{K}_{ww}]\mathbf{q}(s) = -\mathbf{M}_{wc}s^2\boldsymbol{\beta}(s) + q_d[\mathbf{Q}_{ww}(s) \;\; \mathbf{Q}_{wc}(s)]\begin{Bmatrix}\mathbf{q}(s)\\ \boldsymbol{\beta}(s)\end{Bmatrix}, \tag{30}$$

where s is the Laplace variable, $sb_R/V = \mathrm{i}k$.

Minimum state method approximates the aerodynamic force matrices by:

$$[\mathbf{Q}_{ww}(s) \;\; \mathbf{Q}_{wc}(s)] = \mathbf{A}_0 + \frac{b}{V}\mathbf{A}_1 s + \frac{b^2}{V^2}\mathbf{A}_2 s^2 + \mathbf{D}_s\left(\mathbf{I}s - \frac{V}{b}\mathbf{R}_s\right)^{-1}\mathbf{E}_s s, \tag{31}$$

where

$$\mathbf{E}_s = [\mathbf{E}_{ww} \;\; \mathbf{E}_{wc}], \quad \mathbf{A}_j = [\mathbf{A}_{ww_j} \;\; \mathbf{A}_{wc_j}], \quad j = 0, 1, 2 \tag{32}$$

Introducing the following aerodynamic states:

$$\mathbf{X}_a(s) = \left(\mathbf{I}s - \frac{V}{b}\mathbf{R}_s\right)^{-1}(\mathbf{E}_{ww}\mathbf{q}(s) + \mathbf{E}_{wc}\boldsymbol{\beta}(s))s. \tag{33}$$

Now we can obtain the state-space open-loop aeroelastic equation of motion, given by

$$\dot{\mathbf{X}}_{ae}(t) = \mathbf{A}_{ae}\mathbf{X}_{ae}(t) + \mathbf{B}_{ae}\mathbf{U}_{ae}(t), \tag{34}$$

where the matrices in Eq. (34) are given in Appendix D.

The outputs of the aeroelastic plant are taken as acceleration signals, so the output equation used in the design of the control law can be written as

$$\mathbf{Y}_{ae}(t) = \mathbf{C}_{ae}\mathbf{X}_{ae}(t) + \mathbf{D}_{ae}\mathbf{U}_{ae}(t), \tag{35}$$

where

$$\begin{cases} \mathbf{C}_{ae} = \mathbf{S}_{acc}\mathbf{\Phi}\bar{\mathbf{M}}_{ww}^{-1}\left[-(\mathbf{K}_{ww} - q_d\mathbf{A}_{ww_0})\middle| -\left(\mathbf{D}_{ww} - q_d\dfrac{b}{V}\mathbf{A}_{ww_1}\right)\middle| q_d\mathbf{D}_s\right], \\ \mathbf{D}_{ae} = \mathbf{S}_{acc}\mathbf{\Phi}\bar{\mathbf{M}}_{ww}^{-1}\left[q_d\mathbf{A}_{wc_0}\middle| q_d\dfrac{b}{V}\mathbf{A}_{wc_1}\middle| -\left(\mathbf{M}_{wc} - q_d\dfrac{b^2}{V^2}\mathbf{A}_{wc_2}\right)\right], \end{cases} \tag{36}$$

$\mathbf{S}_{acc}$ is the matrix whose elements are related to the locations of sensors.

The dynamic models of the actuators driving the control surfaces are specified by transfer functions having the form:

$$\begin{cases} \dfrac{\beta^{\mathrm{LEI}}(s)}{\beta_{ac}^{\mathrm{LEI}}(s)} = \dfrac{k_{ac}^{\mathrm{LEI}}(\omega_\beta^{\mathrm{LEI}})^2}{(s + a_{ac}^{\mathrm{LEI}})(s^2 + 2\zeta_{ac}^{\mathrm{LEI}}\omega_\beta^{\mathrm{LEI}}s + (\omega_\beta^{\mathrm{LEI}})^2)} = \dfrac{\bar{a}_3^{\mathrm{LEI}}}{s^3 + a_1^{\mathrm{LEI}}s^2 + a_2^{\mathrm{LEI}}s + a_3^{\mathrm{LEI}}}, \\ \dfrac{\beta^{\mathrm{TEI}}(s)}{\beta_{ac}^{\mathrm{TEI}}(s)} = \dfrac{k_{ac}^{\mathrm{TEI}}(\omega_\beta^{\mathrm{TEI}})^2}{(s + a_{ac}^{\mathrm{TEI}})(s^2 + 2\zeta_{ac}^{\mathrm{TEI}}\omega_\beta^{\mathrm{TEI}}s + (\omega_\beta^{\mathrm{TEI}})^2)} = \dfrac{\bar{a}_3^{\mathrm{TEI}}}{s^3 + a_1^{\mathrm{TEI}}s^2 + a_2^{\mathrm{TEI}}s + a_3^{\mathrm{TEI}}}, \\ \dfrac{\beta^{\mathrm{LEO}}(s)}{\beta_{ac}^{\mathrm{LEO}}(s)} = \dfrac{k_{ac}^{\mathrm{LEO}}(\omega_\beta^{\mathrm{LEO}})^2}{(s + a_{ac}^{\mathrm{LEO}})(s^2 + 2\zeta_{ac}^{\mathrm{LEO}}\omega_\beta^{\mathrm{LEO}}s + (\omega_\beta^{\mathrm{LEO}})^2)} = \dfrac{\bar{a}_3^{\mathrm{LEO}}}{s^3 + a_1^{\mathrm{LEO}}s^2 + a_2^{\mathrm{LEO}}s + a_3^{\mathrm{LEO}}}, \\ \dfrac{\beta^{\mathrm{TEO}}(s)}{\beta_{ac}^{\mathrm{TEO}}(s)} = \dfrac{k_{ac}^{\mathrm{TEO}}(\omega_\beta^{\mathrm{TEO}})^2}{(s + a_{ac}^{\mathrm{TEO}})(s^2 + 2\zeta_{ac}^{\mathrm{TEO}}\omega_\beta^{\mathrm{TEO}}s + (\omega_\beta^{\mathrm{TEO}})^2)} = \dfrac{\bar{a}_3^{\mathrm{TEO}}}{s^3 + a_1^{\mathrm{TEO}}s^2 + a_2^{\mathrm{TEO}}s + a_3^{\mathrm{TEO}}}. \end{cases} \tag{37}$$

where the parameters in Eq. (37) are given in Appendix E.

In the design of the controller, in fact, we can specify a two-output controller to reduce the number of output signals of the controller. For this purpose, we use output signal $\beta_{ac}^{\mathrm{EI}}(t)$ to drive the LEI and TEI actuator and output signal $\beta_{ac}^{\mathrm{EO}}(t)$ to drive the LEO and TEO actuator. Hence, we have the following relationships:

$$\beta_{ac}^{\mathrm{LEI}} = k^{\mathrm{LEI}}\beta_{ac}^{\mathrm{EI}}, \quad \beta_{ac}^{\mathrm{TEI}} = k^{\mathrm{TEI}}\beta_{ac}^{\mathrm{EI}}, \quad \beta_{ac}^{\mathrm{LEO}} = k^{\mathrm{LEO}}\beta_{ac}^{\mathrm{EO}}, \quad \beta_{ac}^{\mathrm{TEO}} = k^{\mathrm{TEO}}\beta_{ac}^{\mathrm{EO}}. \tag{38}$$

where k^{LEI}, k^{TEI}, k^{LEO} and k^{LE0} are proportional coefficients. From Eq. (37) and Eq. (38), a state-space realization of the actuator dynamics can be written as

$$\begin{cases} \dot{\mathbf{X}}_{ac}(t) = \mathbf{A}_{ac}\mathbf{X}_{ac}(t) + \mathbf{B}_{ac}\mathbf{U}_{ac}(t), \\ \mathbf{Y}_{ac}(t) = \mathbf{X}_{ac}(t) = \mathbf{U}_{ae}(t). \end{cases} \tag{39}$$

where the matrices in Eq. (39) are given in Appendix F.

5. Control law design

The modern approach to characterizing closed-loop performance objectives is to measure the size of certain closed-loop transfer function matrices using various matrix norms. Matrix norms provide a measure of how large output signals can get for certain classes of input signals. Optimizing these types of performance objectives over the set of stabilizing controllers is the main thrust of recent optimal control theory, such as H_2 and H_∞ control.

In this paper, the control law for flutter suppression is designed using H_∞ synthesis. Fig. 4 shows a block diagram of the H_∞ control design interconnection for the present problem. In Fig. 4, $\mathbf{K}_{\mathrm{con}}(s)$ is the dynamic controller to be determined, $\bar{\mathbf{P}}_{\mathrm{sys}}(s)$ defines the aeroelastic plant of the wing, $\bar{\mathbf{G}}_{\mathrm{act}}(s)$ the actuator system, $\mathbf{Y}_{\mathrm{per}}(t)$ the performance signal, $\mathbf{Y}_{ae}(t)$ the measurement signal. In the design of the control system, performance requirements on the closed-loop system are transformed into the H_∞ framework with the help of weighting or scaling functions. Weights are selected to account for the relative magnitude of signals, their frequency dependence, and their relative importance. The weighting function $\mathbf{W}_{\mathrm{act}}$ is used to limit the magnitude and frequency content of the actuator inputs because the actuator usually works well only in the limited frequency

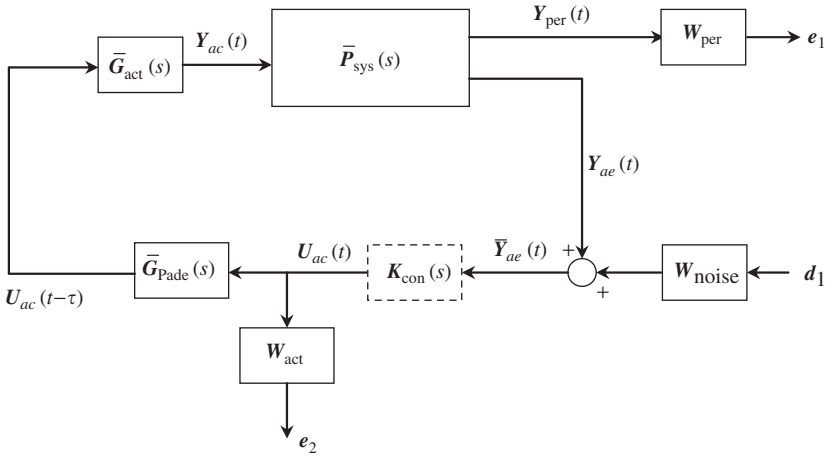

Fig. 4. Block diagram of the H_∞ control.

band and can only provide limited power to actuate the control surface. In a word, $\mathbf{W}_{act}$ is used to shape the penalty on control signal to be used. $\mathbf{W}_{noise}$ represents frequency domain models of sensor noise. Each sensor measurement feedback to the controller has some noise, which is often higher in one frequency range than another. The $\mathbf{W}_{noise}$ weight tries to capture this information, derived from laboratory experiments or based on manufacturer measurements, in the control problem. For example, medium grade accelerometers have substantial noise at low frequency and high frequency. Therefore the corresponding $\mathbf{W}_{noise}$ weight would be larger at low and high frequency and have a smaller magnitude in the mid-frequency range. $\mathbf{W}_{per}$ is the performance weighting function, which can be designed as a low-pass transfer function in order to give a good disturbance rejection performance in the low-frequency region. $\mathbf{U}_{ac}(t)$ is the actual input signal to the actuators.

Since time delay effects play a important role in the stability of the closed-loop system, they are included in the present study. In the frequency domain, time delays can be modeled by the following second order Padé approximation:

$$\bar{\mathbf{G}}_{\mathrm{Pade}}(s) = \begin{bmatrix} G_{\mathrm{Pade}}(s) & 0 \\ 0 & G_{\mathrm{Pade}}(s) \end{bmatrix}, \tag{40}$$

where

$$G_{\mathrm{Pade}}(s) = \mathrm{e}^{-\tau s} \approx \frac{1 - \frac{\tau}{2}s + \frac{\tau^2}{12}s^2}{1 + \frac{\tau}{2}s + \frac{\tau^2}{12}s^2}. \tag{41}$$

and τ denotes time delay. Now the delayed output signal of the controller can be written as

$$\mathbf{U}_{ac}(t-\tau) = \bar{\mathbf{G}}_{\mathrm{Pade}}\mathbf{U}_{ac}(t). \tag{42}$$

The state–space representations for system $\bar{\mathbf{P}}_{sys}(s)$ are:

$$\begin{cases} \dot{\mathbf{X}}_{ae}(t) = \mathbf{A}_{ae}\mathbf{X}_{ae}(t) + \mathbf{B}_{ae}\mathbf{U}_{ae}(t), \\ \left\{\frac{\mathbf{Y}_{per}(t)}{\mathbf{Y}_{ae}(t)}\right\} = \left[\frac{\mathbf{C}_{per}}{\mathbf{C}_{ae}}\right]\mathbf{X}_{ae}(t) + \left[\frac{\mathbf{0}}{\mathbf{D}_{ae}}\right]\mathbf{U}_{ae}(t). \end{cases} \tag{43}$$

where $\mathbf{C}_{per} = \mathbf{S}_{per}\mathbf{\Phi}[\mathbf{I}\ \mathbf{0}\ \mathbf{0}]$, matrix $\mathbf{S}_{per}$ is used to select displacements and twist angle signals at the performance points from displacement vector $\mathbf{W}^{a}$. $\mathbf{Y}_{per}(t)$ is a set of virtual signals used for performance computation.

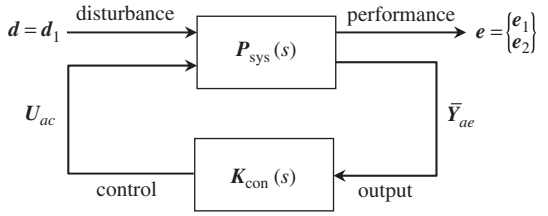

Fig. 5. Block diagram of generalized plant with feedback controller.

The state and output equations of the actuator system $\bar{\mathbf{G}}_{\text{act}}(s)$ are given by

$$\begin{cases} \dot{\mathbf{X}}_{ac}(t) = \mathbf{A}_{ac}\mathbf{X}_{ac}(t) + \mathbf{B}_{ac}\mathbf{U}_{ac}(t-\tau), \\ \mathbf{Y}_{ac}(t) = \mathbf{X}_{ac}(t) = \mathbf{U}_{ae}(t). \end{cases} \tag{44}$$

The open-loop system is obtained by augmentation of the aeroelastic model Eq. (43) with the state–space model of the actuator system Eq. (44), given by

$$\begin{cases} \dot{\mathbf{X}}_{p}(t) = \mathbf{A}_{p}\mathbf{X}_{p}(t) + \mathbf{B}_{p}\mathbf{U}_{ac}(t-\tau), \\ \mathbf{Y}_{p}(t) = \mathbf{Y}_{ae}(t) = \mathbf{C}_{p}\mathbf{X}_{p}(t), \end{cases} \tag{45}$$

where

$$\mathbf{A}_p = \begin{bmatrix} \mathbf{A}_{ae} & \mathbf{B}_{ae} \\ \mathbf{0} & \mathbf{A}_{ac} \end{bmatrix}, \quad \mathbf{B}_p = \begin{bmatrix} \mathbf{0} \\ \mathbf{B}_{ac} \end{bmatrix}, \quad \mathbf{C}_p = [\mathbf{C}_{ae} \;\; \mathbf{D}_{ae}], \quad \mathbf{X}_p = \begin{Bmatrix} \mathbf{X}_{ae} \\ \mathbf{X}_{ac} \end{Bmatrix}.$$

The dynamic H_∞ controller $\mathbf{K}_{\text{con}}(s)$ can be written as

$$\begin{cases} \dot{\mathbf{X}}_{\text{con}}(t) = \mathbf{A}_{\text{con}}\mathbf{X}_{\text{con}}(t) + \mathbf{B}_{\text{con}}\mathbf{Y}_{ae}(t), \\ \mathbf{Y}_{\text{con}}(t) = \mathbf{U}_{ac}(t) = \mathbf{C}_{\text{con}}\mathbf{X}_{\text{con}}(t) + \mathbf{D}_{\text{con}}\mathbf{Y}_{ae}(t). \end{cases} \tag{46}$$

Thus, the equations of motion for the closed-loop system are given by

$$\begin{Bmatrix} \dot{\mathbf{X}}_{p}(t) \\ \dot{\mathbf{X}}_{\text{con}}(t) \end{Bmatrix} = \left[\begin{array}{c|c} \mathbf{A}_p & \mathbf{0} \\ \hline \mathbf{B}_{\text{con}}\mathbf{C}_p & \mathbf{A}_{\text{con}} \end{array}\right] \begin{Bmatrix} \mathbf{X}_{p}(t) \\ \mathbf{X}_{\text{con}}(t) \end{Bmatrix} + \left[\begin{array}{c|c} \mathbf{B}_p\mathbf{D}_{\text{con}}\mathbf{C}_p & \mathbf{B}_p\mathbf{C}_{\text{con}} \\ \hline \mathbf{0} & \mathbf{0} \end{array}\right] \begin{Bmatrix} \mathbf{X}_{p}(t-\tau) \\ \mathbf{X}_{\text{con}}(t-\tau) \end{Bmatrix}. \tag{47}$$

On the basis of the H_∞ interconnection model, an equivalent transfer function of the whole system can be constructed and is denoted by $\mathbf{P}_{\text{sys}}(s)$, as shown in Fig. 5. The H_∞ control of the present aeroelastic system can be stated as: find a dynamic controller $\mathbf{K}_{\text{con}}(s)$ such that the closed-loop system is stable and the performance $||\mathbf{T}_{\mathbf{ed}}(s)||_\infty < \gamma$ is achieved, where $\gamma > 0$ is the prescribed constant, and $||\mathbf{T}_{\mathbf{ed}}(s)||_\infty$ defines the H_∞ norm of the closed-loop system transfer function from the disturbance $\mathbf{d}$ to the performance signal $\mathbf{e}$.

6. The rightmost eigenvalues of the controlled system with time delays

From Eq. (47), we see that the closed-loop system is described by a set of linear delay differential equations. Therefore, to investigate the performance of the designed control system, an efficient algorithm for the computation of the stability of this time delay system should be developed. Here we focus on the computation of the critical time delay of the closed-loop system.

In theoretical aspects of the time delay systems, it is well known that a controlled system is asymptotically stable if all the roots of the corresponding characteristic equation have negative real parts. For a linear time-invariant system with time delays, however, the characteristic equation becomes transcendental due to the exponential functions associated with time delays. The transcendentality brings an infinite number of characteristic roots, which are cumbersome to handle. Due to the high dimensional nature of the present system, the generalized Sturm method described in Ref. [6] is hardly to use. Besides, the perturbation approach

[5] to trace the evolution of the eigenvalues usually gives the wrong result because we can not trace the eigenvalues emerging form infinity.

Delay equations always lead to an infinite number of characteristic roots. However, only a finite number have real parts greater than a given constant. Therefore, stability of the time-delayed system can be determined by computing the rightmost eigenvalues of the DDEs. In this section, the rightmost roots of the controlled aeroelastic system with time delays are computed through the infinitesimal generator approximation. In this section we consider the following linear time-invariant, retarded multiple time-delayed system:

$$\begin{cases} \dot{\mathbf{X}}(t) = \sum_{k=0}^{m} \mathbf{A}_k \mathbf{X}(t-\tau_k), & t>0, \\ \mathbf{X}(t) = \boldsymbol{\varphi}(t), & t \in [-\tau_m, 0], \end{cases} \tag{48}$$

where $0=\tau_0<\tau_1<\ldots<\tau_m$, $\mathbf{A}_k \in \mathbb{R}^{n\times n}$

The characteristic equation of the system in Eq. (48) is:

$$\det(\mathbf{T}(\lambda)) = \det\left(-\lambda\mathbf{I} + \sum_{k=0}^{m} \mathbf{A}_k e^{-\tau_k \lambda}\right) = 0. \tag{49}$$

For the purpose of stability analysis, a numerical method that automatically computes the rightmost roots of Eq. (49) would be of interest. We briefly recall that the solution operator $\mathbf{S}(t)$, $t\geqslant 0$,associated to Eq. (48) is defined by

$$\mathbf{S}(t)\boldsymbol{\varphi}(\theta) = \mathbf{X}_t(\theta), \quad \boldsymbol{\varphi} \in \mathbf{D}_s, \tag{50}$$

where, $\mathbf{D}_s = \mathbf{C}_B([-\tau_m, 0], \mathbb{R}^n)$, $\mathbf{C}_B$ is Banach space, and $\mathbf{X}_t(\theta) = \mathbf{X}(t+\theta), \theta \in [-\tau_m, 0]$. The meaning of the solution operator $\mathbf{S}(t)$ is shown in Fig. 6. Note that the solution operator $\mathbf{S}(t)$ maps $\boldsymbol{\varphi}(-\tau_m)$, $\boldsymbol{\varphi}(0)$ into $\mathbf{X}(t-\tau_m)$ and $\mathbf{X}(t)$, respectively. The infinitesimal generator $\mathbf{A}$ of the solution operator $\mathbf{S}(t)$ is given by

$$\begin{cases} \mathbf{A}\boldsymbol{\phi}(\theta) = \dot{\boldsymbol{\varphi}}(\theta), \quad \boldsymbol{\varphi} \in \mathbf{D}_g(\mathbf{A}), \\ \mathbf{D}_g(\mathbf{A}) = \left\{ \boldsymbol{\varphi} \in \mathbf{D}_s | \dot{\boldsymbol{\varphi}} \in \mathbf{D}_s \text{ and } \dot{\boldsymbol{\varphi}}(0) = \sum_{k=0}^{m} \mathbf{A}_k \boldsymbol{\varphi}(-\tau_k) \right\}. \end{cases} \tag{51}$$

So, Eq. (48) can be restated as the abstract Cauchy problem of the form:

$$\begin{cases} \dfrac{\mathrm{d}\mathbf{X}_t}{\mathrm{d}t} = \mathbf{A}\mathbf{X}_t, \quad t\geqslant 0, \\ \mathbf{X}_0 = \boldsymbol{\varphi}. \end{cases} \tag{52}$$

From the above equations, one can obtain the following result:

$$\det(\mathbf{T}(\lambda)) = 0 \Leftrightarrow \lambda \in \sigma(\mathbf{A}), \tag{53}$$

where $\sigma(\cdot)$ is the spectrum operator. Since the spectrum of the solution generator consists of the characteristic roots, such roots can be computed as the eigenvalues of suitable matrices approximating this infinitesimal generator.

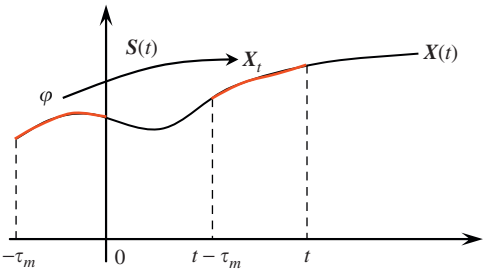

Fig. 6. The solution operator $\mathbf{S}(t)$.

To make a matrix approximation to the infinitesimal generator $\mathbf{A}$, let us consider the following Chebyshev division points in $[-\tau_m, 0]$:

$$\theta_{N,i} = \frac{\tau_m}{2}\left(\cos\left(\mathrm{i}\frac{\pi}{N}\right) - 1\right), \quad i = 0, 1, \ldots, N, \tag{54}$$

where $-\tau_m = \theta_{N,N} < \theta_{N,N-1} < \cdots < \theta_{N,1} < \theta_{N,0} = 0$. Let $\boldsymbol{\varphi}_N$ be an approximation of $\boldsymbol{\varphi}$, and can be written as

$$\boldsymbol{\varphi}_N(\theta) = \sum_{j=0}^{N} [l_j(\theta) \otimes \mathbf{I}_n]\mathbf{f}_j, \tag{55}$$

where $\otimes$ denotes Kronecker products, $l_j(\cdot)$ is the Lagrange interpolating polynomial, and $\mathbf{f}_j = \boldsymbol{\varphi}(\theta_{N,j})$.

On the basis of splicing condition and Eq. (51), one obtains:

$$\begin{cases} (\mathbf{A}\boldsymbol{\varphi})(0) = \dot{\boldsymbol{\varphi}}(0) \simeq \sum\limits_{k=0}^{m} \mathbf{A}_k \boldsymbol{\varphi}_N(-\tau_k) = (\mathbf{A}_N \mathbf{f})_0, \\ (\mathbf{A}\boldsymbol{\varphi})(\theta_{N,i}) = \dot{\boldsymbol{\varphi}}(\theta_{N,i}) \simeq \dot{\boldsymbol{\varphi}}_N(\theta_{N,i}) = (\mathbf{A}_N \mathbf{f})_i, \quad i = 1, 2, \ldots, N, \end{cases} \tag{56}$$

where $\mathbf{A}_N$ denotes the discrete form of $\mathbf{A}$, and $\mathbf{f} = [\mathbf{f}_0^{\mathrm{T}}, \mathbf{f}_1^{\mathrm{T}}, \ldots, \mathbf{f}_N^{\mathrm{T}}]^{\mathrm{T}}$. Obviously, Eq. (56) can be recast as

$$\mathbf{A}_N \begin{Bmatrix} \mathbf{f}_0 \\ \mathbf{f}_1 \\ \vdots \\ \mathbf{f}_N \end{Bmatrix} = \begin{bmatrix} \mathbf{e}_0 & \mathbf{e}_1 & \cdots & \mathbf{e}_N \\ \mathbf{g}_{10} & \mathbf{g}_{11} & \cdots & \mathbf{g}_{1N} \\ \vdots & \vdots & \ddots & \vdots \\ \mathbf{g}_{N0} & \mathbf{g}_{N1} & \cdots & \mathbf{g}_{NN} \end{bmatrix} \begin{Bmatrix} \mathbf{f}_0 \\ \mathbf{f}_1 \\ \vdots \\ \mathbf{f}_N \end{Bmatrix} = \begin{Bmatrix} \sum\limits_{k=0}^{m} \mathbf{A}_k \boldsymbol{\varphi}_N(-\tau_k) \\ \dot{\boldsymbol{\varphi}}_N(\theta_{N,1}) \\ \vdots \\ \dot{\boldsymbol{\varphi}}_N(\theta_{N,N}) \end{Bmatrix}. \tag{57}$$

The elements in matrix $\mathbf{A}_N$ can be obtained as

$$\mathbf{e}_j = \sum_{k=0}^{m} \mathbf{A}_k [l_j(-\tau_k) \otimes \mathbf{I}_n], \quad \mathbf{g}_{ij} = \dot{l}_j(\theta_{N,i}) \otimes \mathbf{I}_n, \quad i = 1, \ldots, N, \ j = 0, 1, \ldots, N. \tag{58}$$

Thus, the rightmost eigenvalues of the above system can be obtained by solving the corresponding eigenvalue problem for matrix $\mathbf{A}_N$. The time delays at which the rightmost eigenvalues become purely imaginary are called critical time delays, they generate potential points for a stability switch of the system.

7. Numerical simulations

7.1. Aerodynamic forces induced by harmonic motions of control surfaces

The wing employed in simulations has a rectangular planform, with a 0.2 m chord and a 1.2 m span. The wing has 20 chord-wise boxes consisting of the lifting surfaces of the main wing (8 boxes), the leading-edge control surface (6 boxes), and the trailing-edge control surface (6 boxes). The wing has 96 span-wise boxes, so a total of 192 aerodynamic boxes are used in simulations.

To validate the developed aerodynamic module for this multiple control surfaces configuration, we attempt to compute the unsteady aerodynamic forces induced by the harmonic pitching motion of control surfaces. For this purpose, we introduce the following four pitching modes of control surfaces:

$$\text{Model-1}: \ \boldsymbol{\beta}(t) = \begin{Bmatrix} +1^\circ \\ +1^\circ \\ +1^\circ \\ +1^\circ \end{Bmatrix} \mathrm{e}^{\mathrm{i}\omega t}, \quad \text{Model-2}: \ \boldsymbol{\beta}(t) = \begin{Bmatrix} +1^\circ \\ +1^\circ \\ -1^\circ \\ +1^\circ \end{Bmatrix} \mathrm{e}^{\mathrm{i}\omega t}. \tag{59a}$$

$$\text{Model-3}: \ \boldsymbol{\beta}(t) = \begin{Bmatrix} -1^\circ \\ +1^\circ \\ +1^\circ \\ +1^\circ \end{Bmatrix} e^{i\omega t}, \quad \text{Model-4}: \ \boldsymbol{\beta}(t) = \begin{Bmatrix} -1^\circ \\ +1^\circ \\ -1^\circ \\ +1^\circ \end{Bmatrix} e^{i\omega t}. \tag{59b}$$

For this simulation, the reduced frequency k is taken as 0.3, and the mach number M_∞ is taken as 0 (incompressible flow). Figs. 7, 8, 9 and 10 illustrate the distribution of the unsteady pressure coefficients induced by the above four pitching modes of control surfaces are computed by using the developed technique in Section 3. It can be seen that due to the complexity of the downwash velocity field, the aerodynamic forces induced by multiple control surfaces are more complex than those by single control surface. Multiple control surfaces can be used to suppress the complex flutter modes due to their different locations in span. Besides, the

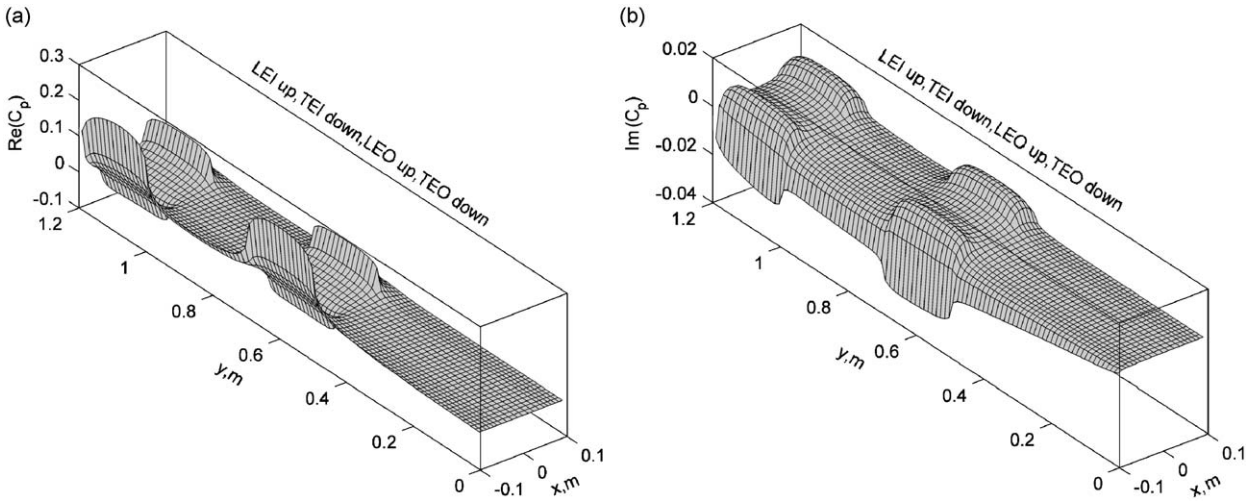

Fig. 7. Distribution of pressure coefficients (Mode-1): (a) real part of the pressure coefficients and (b) imaginary part of the pressure coefficients.

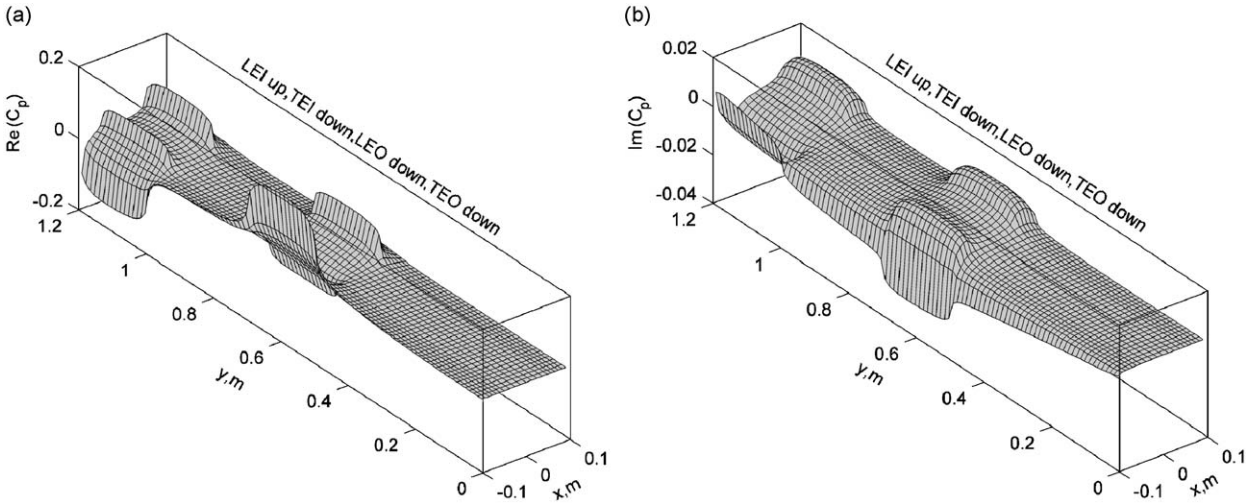

Fig. 8. Distribution of pressure coefficients (Mode-2): (a) real part of the pressure coefficients and (b) imaginary part of the pressure coefficients.

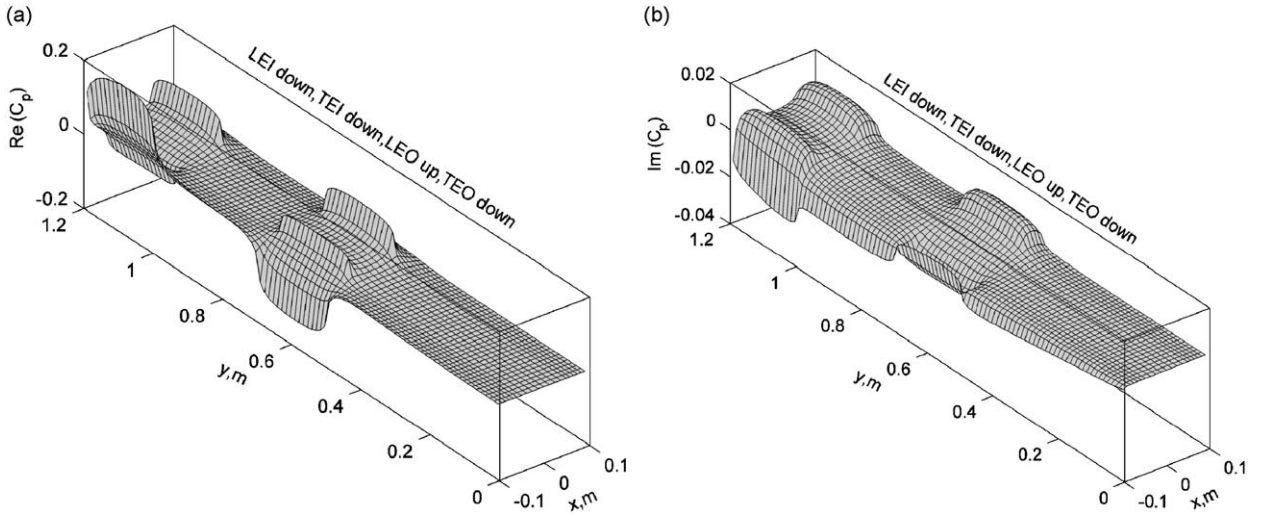

Fig. 9. Distribution of pressure coefficients (Mode-3): (a) real part of the pressure coefficients and (b) imaginary part of the pressure coefficients.

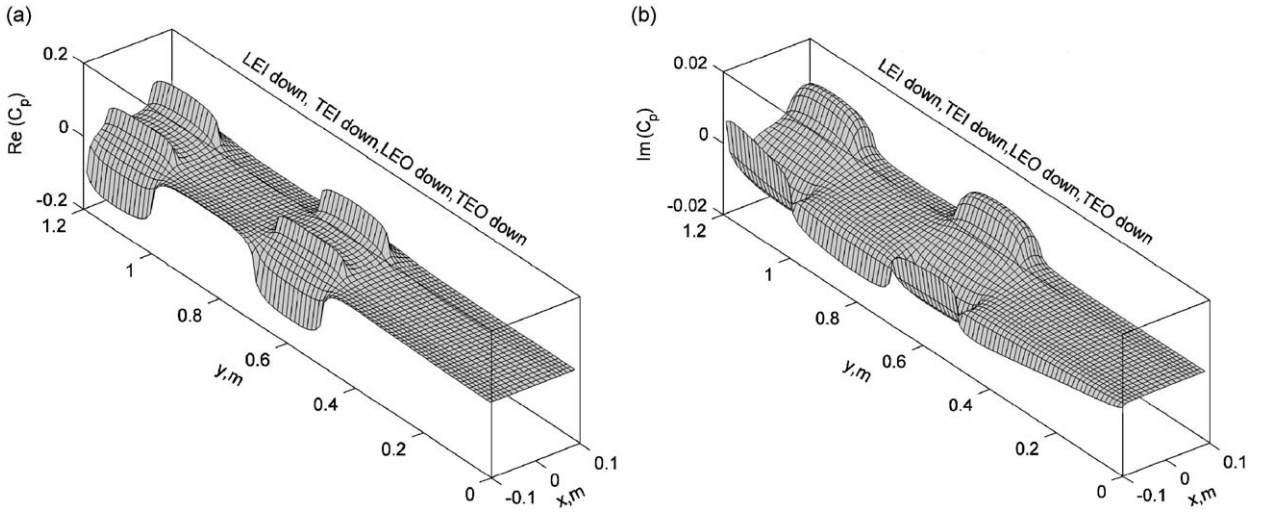

Fig. 10. Distribution of pressure coefficients (Mode-4): (a) real part of the pressure coefficients and (b) imaginary part of the pressure coefficients.

leading-edge control surface may be used to counteract the tendency of a trailing-edge control surface to undergo aeroelastic reversal [13].

7.2. Open-loop stability analysis

Fig. 11 shows a finite element mesh for the wing model consisting of 12 beam-rod elements. The first six natural frequencies of the wing are 1.76, 8.71, 11.2, 25.03, 31.57 and 43.78 Hz, respectively. The transfer function of the discrete actuator is given in Appendix G.

Since the open-loop aeroelastic equation is expressed in the time domain form, flutter analysis can be performed by tracing the eigenvalues of the system matrix at various flow speeds. Here, Mach number is taken as 0.0. Sixteen generalized aerodynamic force matrices at reduced frequency values between $k = 0.0$ and $k = 1.0$ are computed, and the six aerodynamic poles are used in the minimum state approximation. The first

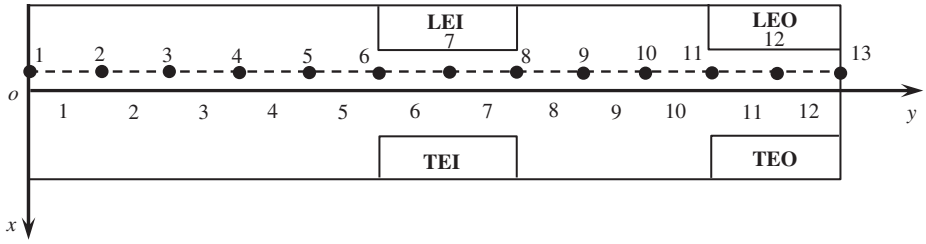

Fig. 11. Finite element model of the wing.

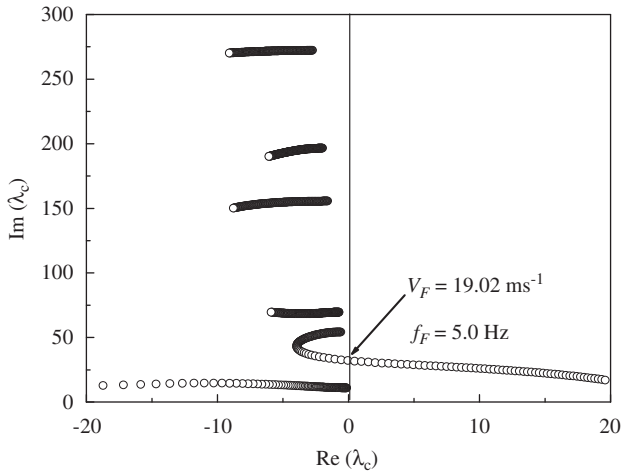

Fig. 12. Open-loop root-locus plot at $M_\infty = 0.0$.

Table 1
Parameters used for controller design.

Controller	Design speed	Output node	Performance node	Design time delay
$\tilde{\mathbf{K}}_{\text{con}}(s)$	$V_d = 23\,\text{ms}^{-1}$	node 7 and node 12	node 11	$\tau_d = 0.014\,\text{s}$

six modes of the wing structure are retained in order to obtain a set of reduced order equations of motion in modal space. So the resulting open-loop aeroelastic model includes 12 structural states, representing 6 low-frequency modes, 6 aerodynamic states, 12 actuator states, leading to a total of 36 states. The root-locus plot for the open-loop flutter analysis is shown in Fig. 12. Obviously, the wing flutters at approximately $V_F = 19.2\,\text{ms}^{-1}$ with frequency of $f_F = 5.0\,\text{Hz}$.

7.3. Stability of the closed-loop aeroelastic system with time delay

The parameters used in synthesizing control law are shown in Table 1. The H_∞ controller is synthesized at the design speed $V_d = 23\,\text{ms}^{-1}$. The acceleration signals taken from node 7 and node 12 in the present finite element model are used as the feedback signals to H_∞ controller. Node 11 is used as a performance node to account for the performance requirement of the closed-loop system. The time delay in control loop is taken as $\tau_d = 0.014\,\text{s}$.

Since the complexity of the control law is not explicitly constrained, the order of the resultant controller is likely to be considerably greater than is truly needed. Therefore, a reduction algorithm applied to the control law can be used to reduce control law complexity with little change in control system performance. In control

theory, eigenvalues define the system stability, whereas Hankel singular values define the "energy" of each state in the system. Keeping larger energy states of a system preserves most of its characteristics in terms of stability, frequency, and time responses. Model reduction technique presented here is based on the Hankel singular values of a system [15]. It can achieve a reduced-order model that preserves the majority of the system characteristics. In this paper, the model reduction technique reduce the original 44-state controller $\mathbf{K}_{\mathrm{con}}(s)$ to a 5-state model, denoted by $\tilde{\mathbf{K}}_{\mathrm{con}}(s)$. The state space form of this reduced order controller $\tilde{\mathbf{K}}_{\mathrm{con}}(s)$ is given in Appendix H.

In practical situations, the delay-independently stable region is usually a very small part in the parameter space of system. If the system parameters do not fall into the delay-independent stable region, the real part of at least one characteristic root changes its sign when the time delay varies. That is, the stability of the controlled system cannot keep unchanged with an increase of time delay. Such a change of stability with time delay is referred to as the stability switch. For the aeroelastic system, the delay-independently stable region only exists in the range of the flow speed which is less than the flutter speed of the open-loop system. Hence, from the practical point of view, this paper only deals with the delay-dependent stability of the system.

With the computation of the rightmost roots of the time-delayed system, the critical time delay of the system at different flow speeds is obtained. As shown in Fig. 13, with the increase of flow speed, the maximum

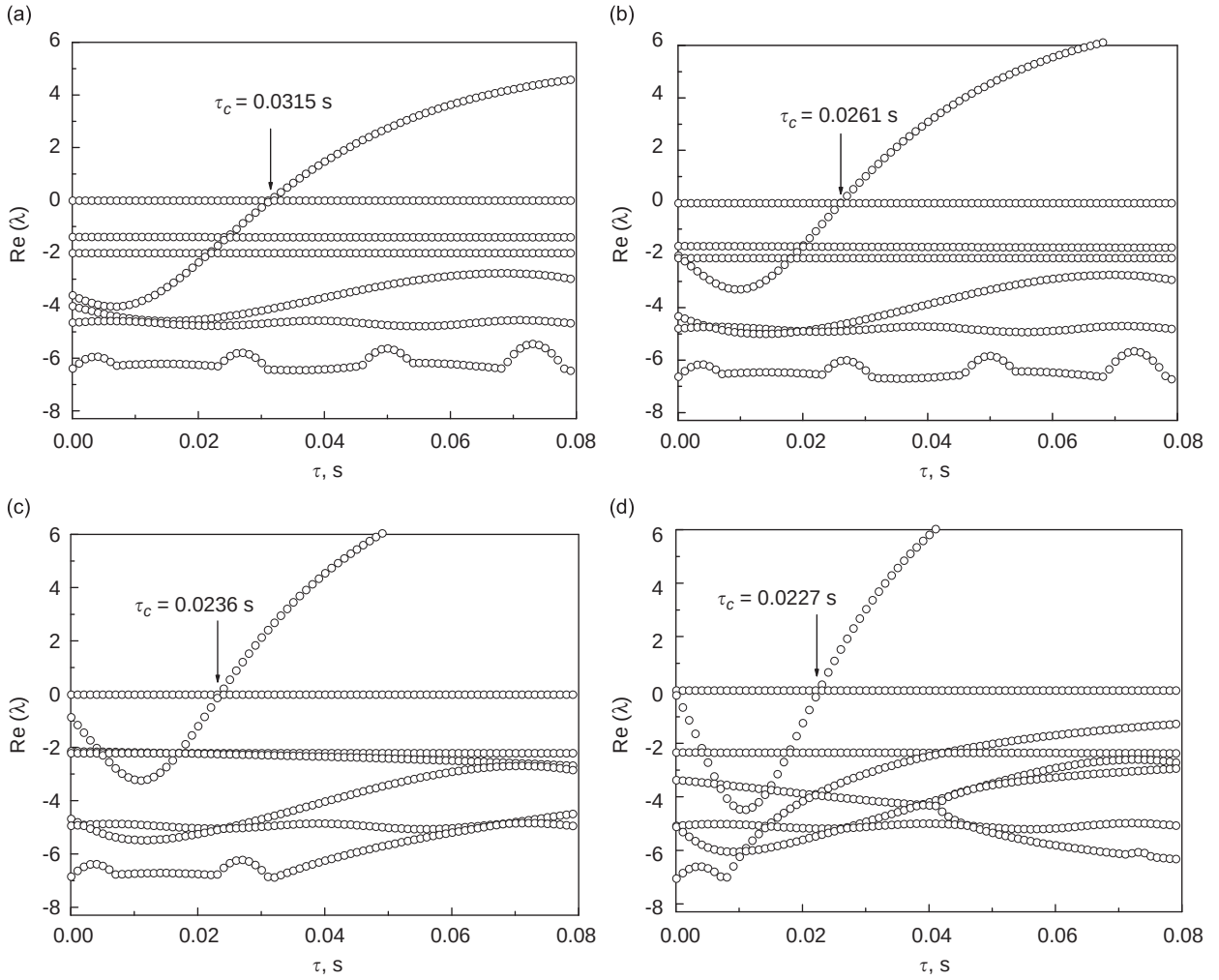

Fig. 13. The rightmost eigenvalues of the closed-loop system with time delay: (a) $V = 20\,\mathrm{ms}^{-1}$, (b) $V = 21\,\mathrm{ms}^{-1}$, (c) $V = 22\,\mathrm{ms}^{-1}$, and (d) $V = 23\,\mathrm{ms}^{-1}$.

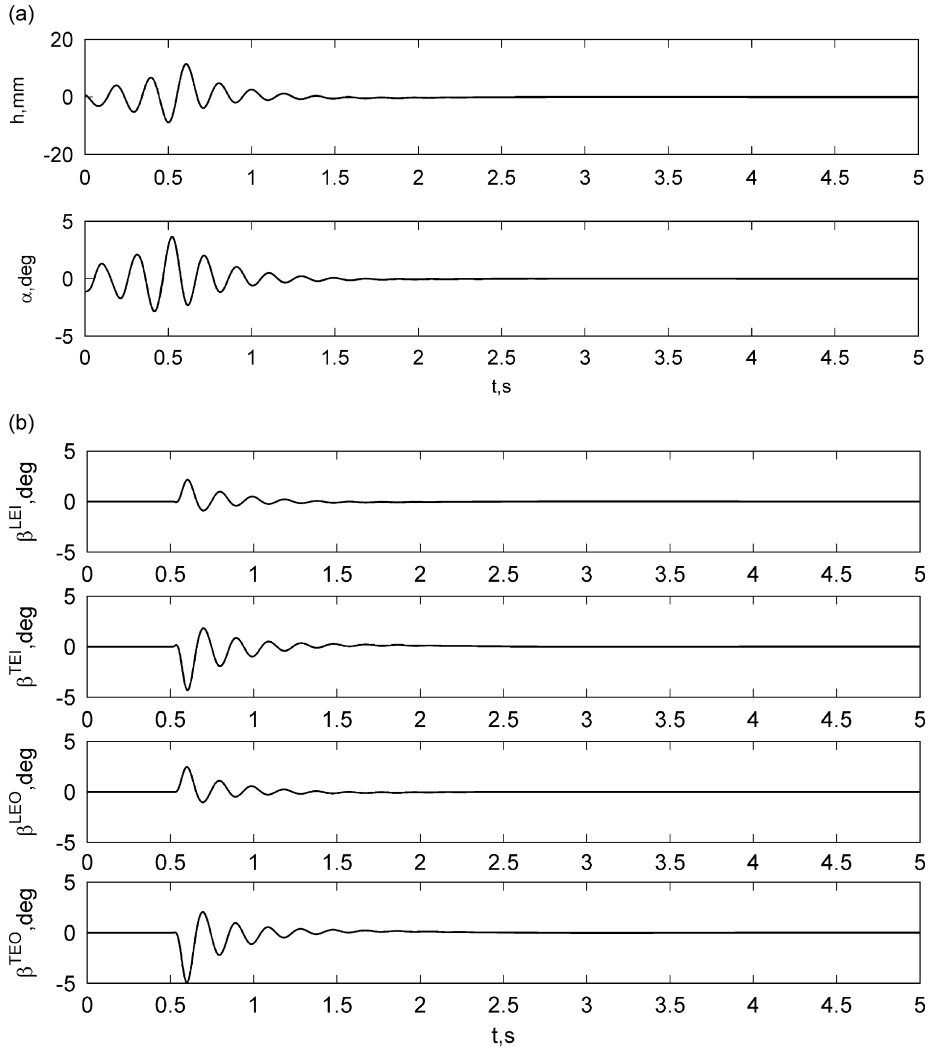

Fig. 14. Time histories of the system at $\tau = 0.014\,\text{s}$, $t_{\text{ctrl}} = 0.5\,\text{s}$, $V = 20\,\text{ms}^{-1}$: (a) responses of node 10 and (b) pitching motions of the control surfaces.

allowable time delay that makes the closed-loop system stable becomes small. The reason is that, with the increase of flow speed, the needed pitching frequency to suppress flutter increases so that the pitching motion is very sensitive to the time delay of system. For flow speed $V = 20\,\text{ms}^{-1}$, the closed-loop system is stable when time delay $\tau \leqslant 0.0315\,\text{s}$, unstable when $\tau > 0.0315\,\text{s}$. That is, the maximum allowable time delay of the system is $\tau = 0.0315\,\text{s}$. In other words, the critical time delay of the closed-loop system at $V = 20\,\text{ms}^{-1}$ is $\tau = 0.0315\,\text{s}$, at which the system undergoes a stability switch.

To validate the result presented in Fig. 13(a), we select a time delay value $\tau = 0.014\,\text{s}$ in the stable interval [0, 0.0315 s] of system, the responses of the system are shown in Fig. 14, where the control activity is initiated at $t_{\text{ctrl}} = 0.5\,\text{s}$. It can be seen from Fig. 14 that flutter is successfully suppressed through the pitching motions of control surfaces.

To illustrate the correctness of the obtained critical time delay values, we increase time delay gradually to see the variations of the stability of system at $V = 20\,\text{ms}^{-1}$. For this purpose, we take time delay τ as 0.02, 0.03 and 0.0325 s, respectively. As shown in Fig. 15, the closed-loop system is stable for both $\tau = 0.02\,\text{s}$ and $\tau = 0.03\,\text{s}$ whereas unstable for $\tau = 0.0325\,\text{s}$. This demonstrates that using the infinitesimal generator approximation of the solution operator, we get the correct critical time delay $\tau_c = 0.0315\,\text{s}$, at which the system undergoes a stability switch.

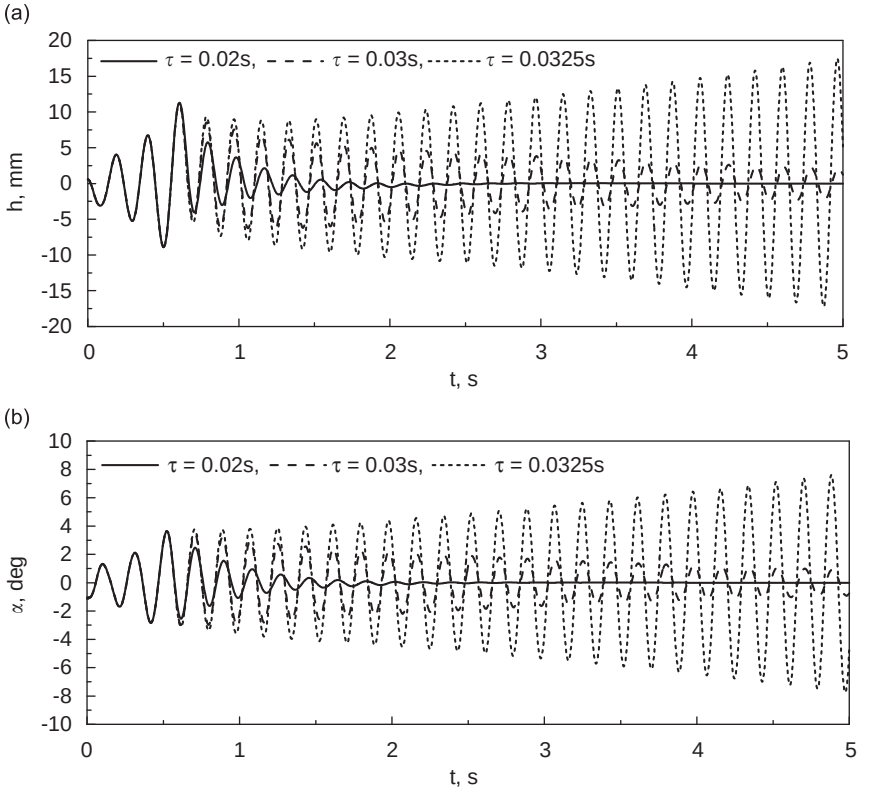

Fig. 15. Time histories of the system at different time delays at $V = 20\,\mathrm{ms}^{-1}$, $t_{\mathrm{ctrl}} = 0.5\,\mathrm{s}$: (a) vertical bending deflection of node 10 and (b) twist angle of node 10.

8. Conclusions

A systematic approach for suppressing flutter of the high aspect-ratio wing with multiple control surfaces is presented. The proposed approach includes unsteady aerodynamic modeling, controller design and stability of the time-delayed aeroelastic system. A computational method suitable for predicting the unsteady aerodynamic forces on the wing with multiple control surfaces is developed, and is validated by numerical simulation. In the controller design, we can see that with the help of the second order Padé approximation of time delay, a dynamic H_∞ controller can be successfully synthesized. Numerical simulations demonstrate that time delays in control system have strong effects on the stability of system. So the non-neglectable time delay effects should be given much attention in the design of the aeroelastic control system for advanced aircraft.

Acknowledgments

This work was supported in part by the China National Funds for Distinguished Young Scientists under Grant no 10825207.

Appendix A. Matrices in Eq. (1)

$$\mathbf{U}_{\mathrm{cont}} = [(x - \bar{c}^{\mathrm{LE}}b)U^{\mathrm{LEI}}(x,y)\ \ (x - \bar{c}^{\mathrm{TE}}b)U^{\mathrm{TEI}}(x,y)\ \ (x - \bar{c}^{\mathrm{LE}}b)U^{\mathrm{LEO}}(x,y)\ \ (x - \bar{c}^{\mathrm{TE}}b)U^{\mathrm{TEO}}(x,y)]^{\mathrm{T}}, \quad \text{(A.1)}$$

$$U^{\mathrm{LEI}}(x,y) = [U_{\mathrm{step}}(x+b) - U_{\mathrm{step}}(x - \bar{c}^{\mathrm{LE}}b)] \cdot [U_{\mathrm{step}}(y - l_a) - U_{\mathrm{step}}(y - l_b)], \quad \text{(A.2)}$$

$$U^{\mathrm{LEO}}(x,y) = [U_{\mathrm{step}}(x+b) - U_{\mathrm{step}}(x - \bar{c}^{\mathrm{LE}}b)] \cdot [U_{\mathrm{step}}(y - l_c) - U_{\mathrm{step}}(y - l_d)], \quad \text{(A.3)}$$

$$U^{\mathrm{TEI}}(x,y)=[U_{\mathrm{step}}(x-\bar{c}^{\mathrm{TE}}b)-U_{\mathrm{step}}(x-b)]\cdot[U_{\mathrm{step}}(y-l_a)-U_{\mathrm{step}}(y-l_b)], \tag{A.4}$$

$$U^{\mathrm{TEO}}(x,y)=[U_{\mathrm{step}}(x-\bar{c}^{\mathrm{TE}}b)-U_{\mathrm{step}}(x-b)]\cdot[U_{\mathrm{step}}(y-l_c)-U_{\mathrm{step}}(y-l_d)], \tag{A.5}$$

$$\boldsymbol{\beta}(t)=[\beta^{\mathrm{LEI}}(t)\ \ \beta^{\mathrm{TEI}}(t)\ \ \beta^{\mathrm{LEO}}(t)\ \ \beta^{\mathrm{TEO}}(t)]^{\mathrm{T}}, \tag{A.6}$$

$$\boldsymbol{\alpha}_{\mathrm{cont}}(y,t)=[f(y,t)\ \ f(y,t)\ \ g(y,t)\ \ g(y,t)]^{\mathrm{T}}. \tag{A.7}$$

Appendix B. Matrices in Eq. (15)

$$\mathbf{h}_{3/4}^{\mathrm{LEI}}=[h(y_{3/4(1)}^{\mathrm{LEI}})\ \ h(y_{3/4(2)}^{\mathrm{LEI}})\cdots h(y_{3/4(n^{\mathrm{LEI}})}^{\mathrm{LEI}})]^{\mathrm{T}},\quad \mathbf{h}_{3/4}^{\mathrm{TEI}}=[h(y_{3/4(1)}^{\mathrm{TEI}})\ \ h(y_{3/4(2)}^{\mathrm{TEI}})\cdots h(y_{3/4(n^{\mathrm{TEI}})}^{\mathrm{TEI}})]^{\mathrm{T}}, \tag{B.1}$$

$$\mathbf{h}_{3/4}^{\mathrm{LEO}}=[h(y_{3/4(1)}^{\mathrm{LEO}})\ \ h(y_{3/4(2)}^{\mathrm{LEO}})\cdots h(y_{3/4(n^{\mathrm{LEO}})}^{\mathrm{LEO}})]^{\mathrm{T}},\quad \mathbf{h}_{3/4}^{\mathrm{TEO}}=[h(y_{3/4(1)}^{\mathrm{TEO}})\ \ h(y_{3/4(2)}^{\mathrm{TEO}})\cdots h(y_{3/4(n^{\mathrm{TEO}})}^{\mathrm{TEO}})]^{\mathrm{T}}, \tag{B.2}$$

$$\boldsymbol{\alpha}_{3/4}^{\mathrm{LEI}}=[\alpha(y_{3/4(1)}^{\mathrm{LEI}})\ \ \alpha(y_{3/4(2)}^{\mathrm{LEI}})\cdots \alpha(y_{3/4(n^{\mathrm{LEI}})}^{\mathrm{LEI}})]^{\mathrm{T}},\quad \boldsymbol{\alpha}_{3/4}^{\mathrm{TEI}}=[\alpha(y_{3/4(1)}^{\mathrm{TEI}})\ \ \alpha(y_{3/4(2)}^{\mathrm{TEI}})\cdots \alpha(y_{3/4(n^{\mathrm{TEI}})}^{\mathrm{TEI}})]^{\mathrm{T}}, \tag{B.3}$$

$$\boldsymbol{\alpha}_{3/4}^{\mathrm{LEO}}=[\alpha(y_{3/4(1)}^{\mathrm{LEO}})\ \ \alpha(y_{3/4(2)}^{\mathrm{LEO}})\cdots \alpha(y_{3/4(n^{\mathrm{LEO}})}^{\mathrm{LEO}})]^{\mathrm{T}},\quad \boldsymbol{\alpha}_{3/4}^{\mathrm{TEO}}=[\alpha(y_{3/4(1)}^{\mathrm{TEO}})\ \ \alpha(y_{3/4(2)}^{\mathrm{TEO}})\cdots \alpha(y_{3/4(n^{\mathrm{TEO}})}^{\mathrm{TEO}})]^{\mathrm{T}}, \tag{B.4}$$

$$\mathbf{D}_{3/4\alpha}^{\mathrm{LEI}}=\mathrm{diag}[x_{3/4(1)}^{\mathrm{LEI}}-\bar{a}b\ \ x_{3/4(2)}^{\mathrm{LEI}}-\bar{a}b\cdots x_{3/4(n^{\mathrm{LEI}})}^{\mathrm{LEI}}-\bar{a}b]^{\mathrm{T}}, \tag{B.5}$$

$$\mathbf{D}_{3/4\alpha}^{\mathrm{TEI}}=\mathrm{diag}[x_{3/4(1)}^{\mathrm{TEI}}-\bar{a}b\ \ x_{3/4(2)}^{\mathrm{TEI}}-\bar{a}b\cdots x_{3/4(n^{\mathrm{TEI}})}^{\mathrm{TEI}}-\bar{a}b], \tag{B.6}$$

$$\mathbf{D}_{3/4\alpha}^{\mathrm{LEO}}=\mathrm{diag}[x_{3/4(1)}^{\mathrm{LEO}}-\bar{a}b\ \ x_{3/4(2)}^{LEO}-\bar{a}b\cdots x_{3/4(n^{LEO})}^{LEO}-\bar{a}b], \tag{B.7}$$

$$\mathbf{D}_{3/4\alpha}^{\mathrm{TEO}}=\mathrm{diag}[x_{3/4(1)}^{\mathrm{TEO}}-\bar{a}b\ \ x_{3/4(2)}^{\mathrm{TEO}}-\bar{a}b\cdots x_{3/4(n^{\mathrm{TEO}})}^{\mathrm{TEO}}-\bar{a}b], \tag{B.8}$$

$$\mathbf{D}_{3/4\beta}^{\mathrm{LEI}}=[x_{3/4(1)}^{\mathrm{LEI}}-\bar{c}^{\mathrm{LE}}b\ \ x_{3/4(2)}^{\mathrm{LEI}}-\bar{c}^{\mathrm{LE}}b\cdots x_{3/4(n^{\mathrm{LEI}})}^{\mathrm{LEI}}-\bar{c}^{\mathrm{LE}}b]^{\mathrm{T}}, \tag{B.9}$$

$$\mathbf{D}_{3/4\beta}^{\mathrm{TEI}}=[x_{3/4(1)}^{\mathrm{TEI}}-\bar{c}^{\mathrm{TE}}b\ \ x_{3/4(2)}^{\mathrm{TEI}}-\bar{c}^{\mathrm{TE}}b\cdots x_{3/4(n^{\mathrm{TEI}})}^{\mathrm{TEI}}-\bar{c}^{\mathrm{TE}}b]^{\mathrm{T}}, \tag{B.10}$$

$$\mathbf{D}_{3/4\beta}^{\mathrm{LEO}}=[x_{3/4(1)}^{\mathrm{LEO}}-\bar{c}^{\mathrm{LE}}b\ \ x_{3/4(2)}^{\mathrm{LEO}}-\bar{c}^{\mathrm{LE}}b\cdots x_{3/4(n^{\mathrm{LEO}})}^{\mathrm{LEO}}-\bar{c}^{\mathrm{LE}}b]^{\mathrm{T}}, \tag{B.11}$$

$$\mathbf{D}_{3/4\beta}^{\mathrm{TEO}}=[x_{3/4(1)}^{\mathrm{TEO}}-\bar{c}^{\mathrm{TE}}b\ \ x_{3/4(2)}^{\mathrm{TEO}}-\bar{c}^{\mathrm{TE}}b\cdots x_{3/4(n^{\mathrm{TEO}})}^{\mathrm{TEO}}-\bar{c}^{\mathrm{TE}}b]^{\mathrm{T}}, \tag{B.12}$$

$$\tilde{\mathbf{D}}_{3/4\beta}^{\mathrm{LEI}}=\mathrm{diag}[x_{3/4(1)}^{\mathrm{LEI}}-\bar{c}^{\mathrm{LE}}b\ \ x_{3/4(2)}^{\mathrm{LEI}}-\bar{c}^{\mathrm{LE}}b\cdots x_{3/4(n^{\mathrm{LEI}})}^{\mathrm{LEI}}-\bar{c}^{\mathrm{LE}}b], \tag{B.13}$$

$$\tilde{\mathbf{D}}_{3/4\beta}^{\mathrm{TEI}}=\mathrm{diag}[x_{3/4(1)}^{\mathrm{TEI}}-\bar{c}^{\mathrm{TE}}b\ \ x_{3/4(2)}^{\mathrm{TEI}}-\bar{c}^{\mathrm{TE}}b\cdots x_{3/4(n^{\mathrm{TEI}})}^{\mathrm{TEI}}-\bar{c}^{\mathrm{TE}}b], \tag{B.14}$$

$$\tilde{\mathbf{D}}_{3/4\beta}^{\mathrm{LEO}}=\mathrm{diag}[x_{3/4(1)}^{\mathrm{LEO}}-\bar{c}^{\mathrm{LE}}b\ \ x_{3/4(2)}^{\mathrm{LEO}}-\bar{c}^{\mathrm{LE}}b\cdots x_{3/4(n^{\mathrm{LEO}})}^{\mathrm{LEO}}-\bar{c}^{\mathrm{LE}}b], \tag{B.15}$$

$$\tilde{\mathbf{D}}_{3/4\beta}^{\mathrm{TEO}}=\mathrm{diag}[x_{3/4(1)}^{\mathrm{TEO}}-\bar{c}^{\mathrm{TE}}b\ \ x_{3/4(2)}^{\mathrm{TEO}}-\bar{c}^{\mathrm{TE}}b\cdots x_{3/4(n^{\mathrm{TEO}})}^{\mathrm{TEO}}-\bar{c}^{\mathrm{TE}}b], \tag{B.16}$$

$$\mathbf{f}_{3/4}^{\mathrm{LEI}}=[f(y_{3/4(1)}^{\mathrm{LEI}},t)\ \ f(y_{3/4(2)}^{\mathrm{LEI}},t)\cdots f(y_{3/4(n^{\mathrm{LEI}})}^{\mathrm{LEI}},t)]^{\mathrm{T}}, \tag{B.17}$$

$$\mathbf{f}_{3/4}^{\mathrm{TEI}}=[f(y_{3/4(1)}^{\mathrm{TEI}},t)\ \ f(y_{3/4(2)}^{\mathrm{TEI}},t)\cdots f(y_{3/4(n^{\mathrm{TEI}})}^{\mathrm{TEI}},t)]^{\mathrm{T}}, \tag{B.18}$$

$$\mathbf{g}_{3/4}^{\mathrm{LEO}}=[g(y_{3/4(1)}^{\mathrm{LEO}},t)\ \ g(y_{3/4(2)}^{\mathrm{LEO}},t)\cdots g(y_{3/4(n^{\mathrm{LEO}})}^{\mathrm{LEO}},t)]^{\mathrm{T}}, \tag{B.19}$$

$$\mathbf{g}_{3/4}^{\mathrm{TEO}}=[g(y_{3/4(1)}^{\mathrm{TEO}},t)\ \ g(y_{3/4(2)}^{\mathrm{TEO}},t)\cdots g(y_{3/4(n^{\mathrm{TEO}})}^{\mathrm{TEO}},t)]^{\mathrm{T}}, \tag{B.20}$$

where n^{LEI}, n^{TEI}, n^{LEO} and n^{TEO} are the number of the aerodynamic boxes on LEI, TEI, LEO and TEO control surfaces, respectively.

Appendix C. Matrices in Eq. (19)

$$\mathbf{D}_{3/4}^{h\alpha}(k)=\begin{bmatrix} -\mathbf{A}_{3/4\alpha}^{\mathrm{LEI}}-\mathbf{A}_{3/4f}^{\mathrm{LEI}}+\dfrac{\mathrm{i}k}{b_R}(\mathbf{A}_{3/4h}^{\mathrm{LEI}}-\mathbf{D}_{3/4\alpha}^{\mathrm{LEI}}\mathbf{A}_{3/4\alpha}^{\mathrm{LEI}}-\bar{\mathbf{D}}_{3/4\beta}^{\mathrm{LEI}}\mathbf{A}_{3/4f}^{\mathrm{LEI}}) \\ -\mathbf{A}_{3/4\alpha}^{\mathrm{TEI}}-\mathbf{A}_{3/4f}^{\mathrm{TEI}}+\dfrac{\mathrm{i}k}{b_R}(\mathbf{A}_{3/4h}^{\mathrm{TEI}}-\mathbf{D}_{3/4\alpha}^{\mathrm{TEI}}\mathbf{A}_{3/4\alpha}^{\mathrm{TEI}}-\bar{\mathbf{D}}_{3/4\beta}^{\mathrm{TEI}}\mathbf{A}_{3/4f}^{\mathrm{TEI}}) \\ -\mathbf{A}_{3/4\alpha}^{\mathrm{LEO}}-\mathbf{A}_{3/4g}^{\mathrm{LEO}}+\dfrac{\mathrm{i}k}{b_R}(\mathbf{A}_{3/4h}^{\mathrm{LEO}}-\mathbf{D}_{3/4\alpha}^{\mathrm{LEO}}\mathbf{A}_{3/4\alpha}^{\mathrm{LEO}}-\bar{\mathbf{D}}_{3/4\beta}^{\mathrm{LEO}}\mathbf{A}_{3/4g}^{\mathrm{LEO}}) \\ -\mathbf{A}_{3/4\alpha}^{\mathrm{TEO}}-\mathbf{A}_{3/4g}^{\mathrm{TEO}}+\dfrac{\mathrm{i}k}{b_R}(\mathbf{A}_{3/4h}^{\mathrm{TEO}}-\mathbf{D}_{3/4\alpha}^{\mathrm{TEO}}\mathbf{A}_{3/4\alpha}^{\mathrm{TEO}}-\bar{\mathbf{D}}_{3/4\beta}^{\mathrm{TEO}}\mathbf{A}_{3/4g}^{\mathrm{TEO}}) \end{bmatrix}, \tag{C.1}$$

$$\mathbf{D}_{3/4}^{\beta}(k)=\begin{bmatrix} \mathbf{I}_{\beta}^{\mathrm{LEI}}+\dfrac{\mathrm{i}k}{b_R}\mathbf{D}_{3/4\beta}^{\mathrm{LEI}} & \mathbf{0} & \mathbf{0} & \mathbf{0} \\ \mathbf{0} & \mathbf{I}_{\beta}^{\mathrm{TEI}}+\dfrac{\mathrm{i}k}{b_R}\mathbf{D}_{3/4\beta}^{\mathrm{TEI}} & \mathbf{0} & \mathbf{0} \\ \mathbf{0} & \mathbf{0} & \mathbf{I}_{\beta}^{\mathrm{LEO}}+\dfrac{\mathrm{i}k}{b_R}\mathbf{D}_{3/4\beta}^{\mathrm{LEO}} & \mathbf{0} \\ \mathbf{0} & \mathbf{0} & \mathbf{0} & \mathbf{I}_{\beta}^{\mathrm{TEO}}+\dfrac{\mathrm{i}k}{b_R}\mathbf{D}_{3/4\beta}^{\mathrm{TEO}} \end{bmatrix}. \tag{C.2}$$

Appendix D. Matrices in Eq. (34)

$$\mathbf{A}_{ae}=\left[\begin{array}{c|c|c} \mathbf{0} & \mathbf{I} & \mathbf{0} \\ \hline -\bar{\mathbf{M}}_{ww}^{-1}(\mathbf{K}_{ww}-q_d\mathbf{A}_{ww_0}) & -\bar{\mathbf{M}}_{ww}^{-1}\mathbf{D}_{ww}-q_d\frac{b}{V}\mathbf{A}_{ww_1} & q_d\bar{\mathbf{M}}_{ww}^{-1}\mathbf{D}_s \\ \hline \mathbf{0} & \mathbf{E}_{ww} & \frac{V}{b}\mathbf{R}_s \end{array}\right], \tag{D.1}$$

$$\mathbf{B}_{ae}=\left[\begin{array}{c|c|c} \mathbf{0} & \mathbf{0} & \mathbf{0} \\ \hline q_d\bar{\mathbf{M}}_{ww}^{-1}\mathbf{A}_{wc_0} & q_d\frac{b}{V}\bar{\mathbf{M}}_{ww}^{-1}\mathbf{A}_{wc_1} & -\bar{\mathbf{M}}_{ww}^{-1}\left(\mathbf{M}_{wc}-q_d\frac{b^2}{V^2}\mathbf{A}_{wc_2}\right) \\ \hline \mathbf{0} & \mathbf{E}_{wc} & \mathbf{0} \end{array}\right], \tag{D.2}$$

$$\bar{\mathbf{M}}_{ww}=\mathbf{M}_{ww}-q_d\frac{b^2}{V^2}\mathbf{A}_{ww_2},\quad \mathbf{X}_{ae}(t)=\begin{Bmatrix}\mathbf{q}(t)\\ \dot{\mathbf{q}}(t)\\ \mathbf{X}_a(t)\end{Bmatrix},\quad \mathbf{U}_{ae}(t)=\begin{Bmatrix}\boldsymbol{\beta}(t)\\ \dot{\boldsymbol{\beta}}(t)\\ \ddot{\boldsymbol{\beta}}(t)\end{Bmatrix}. \tag{D.3}$$

Appendix E. Parameters in Eq. (37)

$$\bar{a}_3^{\mathrm{LEI}}=k_{ac}^{\mathrm{LEI}}(\omega_{\beta}^{\mathrm{LEI}})^2,\quad \bar{a}_3^{\mathrm{TEI}}=k_{ac}^{\mathrm{TEI}}(\omega_{\beta}^{\mathrm{TEI}})^2,\quad \bar{a}_3^{\mathrm{LEO}}=k_{ac}^{\mathrm{LEO}}(\omega_{\beta}^{\mathrm{LEO}})^2,\quad \bar{a}_3^{\mathrm{TEO}}=k_{ac}^{\mathrm{TEO}}(\omega_{\beta}^{\mathrm{TEO}})^2, \tag{E.1}$$

$$a_1^{\mathrm{LEI}}=a_{ac}^{\mathrm{LEI}}+2\zeta_{ac}^{\mathrm{LEI}}\omega_{\beta}^{\mathrm{LEI}},\quad a_1^{\mathrm{TEI}}=a_{ac}^{\mathrm{TEI}}+2\zeta_{ac}^{\mathrm{TEI}}\omega_{\beta}^{\mathrm{TEI}}, \tag{E.2}$$

$$a_1^{\mathrm{LEO}}=a_{ac}^{\mathrm{LEO}}+2\zeta_{ac}^{\mathrm{LEO}}\omega_{\beta}^{\mathrm{LEO}},\quad a_1^{\mathrm{TEO}}=a_{ac}^{\mathrm{TEO}}+2\zeta_{ac}^{\mathrm{TEO}}\omega_{\beta}^{\mathrm{TEO}}, \tag{E.3}$$

$$a_2^{\mathrm{LEI}} = (\omega_\beta^{\mathrm{LEI}})^2 + 2a_{ac}^{\mathrm{LEI}}\zeta_{ac}^{\mathrm{LEI}}\omega_\beta^{\mathrm{LEI}}, \quad a_2^{\mathrm{TEI}} = (\omega_\beta^{\mathrm{TEI}})^2 + 2a_{ac}^{\mathrm{TEI}}\zeta_{ac}^{\mathrm{TEI}}\omega_\beta^{\mathrm{TEI}}, \tag{E.4}$$

$$a_2^{\mathrm{LEO}} = (\omega_\beta^{\mathrm{LEO}})^2 + 2a_{ac}^{\mathrm{LEO}}\zeta_{ac}^{\mathrm{LEO}}\omega_\beta^{\mathrm{LEO}}, \quad a_2^{\mathrm{TEO}} = (\omega_\beta^{\mathrm{TEO}})^2 + 2a_{ac}^{\mathrm{TEO}}\zeta_{ac}^{\mathrm{TEO}}\omega_\beta^{\mathrm{TEO}}, \tag{E.5}$$

$$a_3^{\mathrm{LEI}} = a_{ac}^{\mathrm{LEI}}(\omega_\beta^{\mathrm{LEI}})^2, \quad a_3^{\mathrm{TEI}} = a_{ac}^{\mathrm{TEI}}(\omega_\beta^{\mathrm{TEI}})^2, \quad a_3^{\mathrm{LEO}} = a_{ac}^{\mathrm{LEO}}(\omega_\beta^{\mathrm{LEO}})^2, \quad a_3^{\mathrm{TEO}} = a_{ac}^{\mathrm{TEO}}(\omega_\beta^{\mathrm{TEO}})^2, \tag{E.6}$$

where $\beta_{ac}^{\mathrm{LEI}}$, k_{ac}^{LEI}, $\zeta_{ac}^{\mathrm{LEI}}$, and $\omega_\beta^{\mathrm{LEI}}$ are the servo-commanded rotation angle, steady-state gain, damping ratio and uncoupled natural frequency of the LEI actuator, respectively.

Appendix F. Matrices in Eq. (39)

$$\mathbf{A}_{ac} = \begin{bmatrix} \mathbf{0}_{4\times4} & \mathbf{I}_{4\times4} & \mathbf{0}_{4\times4} \\ \mathbf{0}_{4\times4} & \mathbf{0}_{4\times4} & \mathbf{I}_{4\times4} \\ \mathbf{A}_{ac3} & \mathbf{A}_{ac2} & \mathbf{A}_{ac1} \end{bmatrix}, \quad \mathbf{B}_{ac} = \begin{bmatrix} \mathbf{0}_{8\times2} \\ \bar{\mathbf{B}}_{ac3} \end{bmatrix}, \quad \bar{\mathbf{B}}_{ac3} = \begin{bmatrix} \bar{a}_3^{\mathrm{LEI}}k^{\mathrm{LEI}} & 0 \\ \bar{a}_3^{\mathrm{TEI}}k^{\mathrm{TEI}} & 0 \\ 0 & \bar{a}_3^{\mathrm{LEO}}k^{\mathrm{LEO}} \\ 0 & \bar{a}_3^{\mathrm{TEO}}k^{\mathrm{TEO}} \end{bmatrix}, \tag{F.1}$$

$$\mathbf{A}_{ac3} = \mathrm{diag}[-a_3^{\mathrm{LEI}} \ -a_3^{\mathrm{TEI}} \ -a_3^{\mathrm{LEO}} \ -a_3^{\mathrm{TEO}}], \tag{F.2}$$

$$\mathbf{A}_{ac2} = \mathrm{diag}[-a_2^{\mathrm{LEI}} \ -a_2^{\mathrm{TEI}} \ -a_2^{\mathrm{LEO}} \ -a_2^{\mathrm{TEO}}], \tag{F.3}$$

$$\mathbf{A}_{ac1} = \mathrm{diag}[-a_1^{\mathrm{LEI}} \ -a_1^{\mathrm{TEI}} \ -a_1^{\mathrm{LEO}} \ -a_1^{\mathrm{TEO}}], \tag{F.4}$$

$$\mathbf{U}_{ac}(t) = \begin{Bmatrix} \beta_{ac}^{\mathrm{EI}}(t) \\ \beta_{ac}^{\mathrm{EO}}(t) \end{Bmatrix}, \quad \mathbf{X}_{ac}(t) = \mathbf{U}_{ae}(t) = \begin{Bmatrix} \boldsymbol{\beta}(t) \\ \dot{\boldsymbol{\beta}}(t) \\ \ddot{\boldsymbol{\beta}}(t) \end{Bmatrix}. \tag{F.5}$$

Appendix G. The transfer function of the discrete actuator

The third order transfer function of the actuator driving the control surface is defined as

$$\frac{\beta^{\mathrm{LEI}}(s)}{\beta_{ac}^{\mathrm{LEI}}(s)} = \frac{\beta^{\mathrm{TEI}}(s)}{\beta_{ac}^{\mathrm{TEI}}(s)} = \frac{\beta^{\mathrm{LEO}}(s)}{\beta_{ac}^{\mathrm{LEO}}(s)} = \frac{\beta^{\mathrm{TEO}}(s)}{\beta_{ac}^{\mathrm{TEO}}(s)} = \frac{3.2\mathrm{e}6}{s^3 + 420s^2 + 1.68\mathrm{e}5s + 3.2\mathrm{e}6}, \tag{G.1}$$

where $\beta_{ac}^{\mathrm{LEI}}$, $\beta_{ac}^{\mathrm{TEI}}$, $\beta_{ac}^{\mathrm{LEO}}$ and $\beta_{ac}^{\mathrm{TEO}}$ are input signals of the actuators.

Appendix H. The state space form (see Eq. (46)) of the reduced-order controller $\bar{\mathbf{K}}_{\mathbf{con}}(s)$

$$\mathbf{A}_{\mathrm{con}} = \begin{bmatrix} -1.0359 & 1.1497 & 1.6354 & -0.4187 & 2.4177 \\ -1.1498 & -0.2577 & -0.4941 & 0.3689 & -1.6363 \\ -1.6352 & -0.4947 & -0.9685 & 0.8668 & -3.5518 \\ -0.3752 & -0.3399 & -0.7980 & -1.2143 & 69.7664 \\ -2.4070 & -1.6272 & -3.5395 & -68.9785 & -32.4435 \end{bmatrix}, \tag{H.1}$$

$$\mathbf{B}_{\mathrm{con}} = \begin{bmatrix} -0.1798 & -0.5905 \\ -0.0628 & -0.1891 \\ -0.1055 & -0.3173 \\ 0.0461 & -0.1370 \\ -0.3056 & -0.6260 \end{bmatrix}, \tag{H.2}$$

$$\mathbf{C}_{\text{con}} = \begin{bmatrix} -0.3992 & 0.1336 & 0.2197 & -0.0358 & 0.5133 \\ -0.4708 & 0.1478 & 0.2521 & -0.1400 & 0.4710 \end{bmatrix}, \tag{H.3}$$

$$\mathbf{D}_{\text{con}} = \begin{bmatrix} 0 & 0 \\ 0 & 0 \end{bmatrix}. \tag{H.4}$$

References

[1] L. Librescu, P. Marzocca, Advances in the linear/nonlinear control of aeroelastic structural systems, *Acta Mechanica* 178 (2002) 147–186.

[2] D. Borglund, J. Kuttenkeuler, Active wing flutter suppression using a trailing-edge flap, *Journal of Fluids and Structures* 16 (3) (2002) 271–294.

[3] J.H. Han, J. Tani, Active flutter suppression of a lifting surface using piezoelectric actuation and modern control theory, *Journal of Sound and Vibration* 291 (2006) 706–722.

[4] M. Andrighettoni, P. Mantegazza, Multi-input/multi-output adaptive active flutter suppression for a wing model, *Journal of Aircraft* 35 (3) (1998) 462–469.

[5] H.Y. Hu, E.H. Dowell, L.N. Virgin, Stability estimation of high dimensional vibrating system under state delay feedback control, *Journal of Sound and Vibration* 214 (1998) 497–511.

[6] Z.H. Wang, H.Y. Hu, Stability switches of the time delayed dynamic systems with unknown parameters, *Journal of Sound and Vibration* 233 (2000) 215–233.

[7] M. Ramesh, S. Narayanan, Controlling chaotic motions in a two-dimensional airfoil using time-delayed feedback, *Journal of Sound and Vibration* 239 (2001) 1037–1049.

[8] Y. Yuan, P. Yu, L. Librescu, P. Marzocca, Aeroelasticity of time-delayed feedback control of two-dimensional supersonic lifting surfaces, *Journal of Guidance Control and Dynamics* 27 (2004) 795–803.

[9] P. Marzocca, L. Librescu, Time-delay effects on linear/nonlinear feedback control of simple aeroelastic systems, *Journal of Guidance Control and Dynamics* 28 (2005) 53–62.

[10] L. Librescu, P. Marzocca, Aeroelasticity of 2D lifting surfaces with time-delayed feedback control, *Journal of Fluids and Structures* 20 (2005) 197–215.

[11] P. Yu, Z. Chen, L. Librescu, P. Marzocca, Implications of time-delayed feedback control on limit cycle oscillation of a two-dimensional supersonic lifting surface, *Journal of Sound and Vibration* 304 (2007) 974–986.

[12] V. Mukhopadhyay, Flutter suppression control law design and testing for the active flexible wing, *Journal of Aircraft* 32 (1) (1995) 45–51.

[13] E.H. Dowell, D.B. Bliss, Aeroelastic wing with leading and trailing-edge control surfaces, *Journal of Aircraft* 40 (3) (2003) 559–565.

[14] E. Albano, W.P. Rodden, A doublet-lattice method for calculating lifting disturbances on oscillating surfaces in subsonic flows, *AIAA Journal* 7 (2) (1969) 279–285.

[15] G. Obinata, B.D.O. Anderson, *Model Reduction for Control System Design*, Springer-Verlag, London, 2001.